

# NON-LTE MODELS AND THEORETICAL SPECTRA OF ACCRETION DISKS IN ACTIVE GALACTIC NUCLEI. IV. EFFECTS OF COMPTON SCATTERING AND METAL OPACITIES

IVAN HUBENY

AURA/NOAO, NASA Goddard Space Flight Center, Code 681, Greenbelt, MD 20771. hubeny@tlsty.gsfc.nasa.gov

OMER BLAES

Department of Physics, University of California, Santa Barbara, CA 93106. blaes@gemini.physics.ucsb.edu

JULIAN H. KROLIK

Department of Physics and Astronomy, Johns Hopkins University, Baltimore, MD 21218. jhk@tarkus.pha.jhu.edu

AND

ERIC AGOL<sup>1</sup>

Department of Physics and Astronomy, Johns Hopkins University, Baltimore, MD 21218. agol@woody.tapir.caltech.edu

*To appear in The Astrophysical Journal*

## ABSTRACT

We extend our models of the vertical structure and emergent radiation field of accretion disks around supermassive black holes described in previous papers of this series. Our models now include both a self-consistent treatment of Compton scattering and the effects of continuum opacities of the most important metal species (C, N, O, Ne, Mg, Si, S, Ar, Ca, Fe, Ni). With these new effects incorporated, we compute the predicted spectrum from black holes accreting at nearly the Eddington luminosity ( $L/L_{\text{Edd}} \approx 0.3$ ) and central masses of  $10^6$ ,  $10^7$ , and  $10^8 M_{\odot}$ . We also consider two values of the Shakura-Sunyaev  $\alpha$  parameter, 0.1 and 0.01, but in contrast to our previous papers, we consider a kinematic viscosity which is independent of depth.

Although it has little effect when  $M > 10^8 M_{\odot}$ , Comptonization grows in importance as the central mass decreases and the central temperature rises. It generally produces an increase in temperature with height in the uppermost layers of hot atmospheres. Compared to models with coherent electron scattering, Comptonized models have enhanced extreme ultraviolet/soft X-ray emission, but they also have a more sharply declining spectrum at very high frequencies. Comptonization also smears the hydrogen and the He II Lyman edges. The effects of metals on the overall spectral energy distribution are smaller than the effects of Comptonization for these parameters. Compared to pure hydrogen-helium models, models with metal continuum opacities have reduced flux in the high frequency tail, except at the highest frequencies, where the flux is very low. Metal photoionization edges are not present in the overall disk-integrated model spectra.

The viscosity parameter  $\alpha$  has a more dramatic effect on the emergent spectrum than do metal continuum opacities. As  $\alpha$  increases (and therefore the disk column density decreases), the flux at both the high and low frequency extremes of the spectrum increases, while the flux near the peak decreases. Multitemperature blackbodies are a very poor approximation to accretion disk spectra in the soft X-ray region, and such crude modeling may greatly overestimate the accretion luminosity required to explain observed soft X-ray excesses in active galactic nuclei. In addition to our new grid of models, we also present a simple analytic prescription for the vertical temperature structure of the disk in the presence of Comptonization, and show under what conditions a hot outer layer (a corona) is formed.

*Subject headings:* accretion, accretion disks—galaxies:active—galaxies:nuclei—radiative transfer

## 1. INTRODUCTION

In previous papers of this series (Hubeny & Hubeny 1997, 1998; Hubeny et al. 2000; hereafter referred to as Papers I, II, and III, respectively), we computed a series of models of accretion disks around supermassive black holes appropriate for quasars and active galactic nuclei (AGN). The models included a set of 1-D vertical structure calculations for the individual annuli of the disk. We solved self-consistently the equations of vertical hydrostatic equilibrium, energy balance, radiative transfer, and, since we did not assume local thermodynamic equilibrium (LTE), the set of statistical equilibrium equations for selected energy levels of various species of atoms and ions. In these previous models, we considered a simple H-He chemical composition, and we assumed that electron scattering was coherent (i.e., Thomson scattering).

In the present paper, we refine the previous modeling procedure by relaxing these two limiting approximations. We now incorporate metals, and we include the effects of incoherent electron scattering, i.e. Compton scattering. Both of these effects are expected to modify the emergent spectrum of individual hot annuli which emit predominantly in the extreme ultraviolet and soft X-rays. Excess emission above a power law extending down from the hard X-rays is widely observed in many classes of AGN, from Seyferts to quasars (e.g. Turner & Pounds 1989). The origin of this emission remains unclear, but it has been proposed to be thermal, Comptonized emission from hot portions of an accretion disk (e.g. Czerny & Elvis 1987; Ross, Fabian & Mineshige 1992). In addition, fluorescent line emission and Compton reflection humps are observed in AGN (Nandra & Pounds 1994) and appear to be at least partly the result of exter-

<sup>1</sup>present address: California Institute of Technology, Pasadena, CA 91125

nal illumination of the disk by hard X-rays from a hot, coronal region somewhere in the vicinity. The effects of Compton scattering and metal opacities within the disk itself are crucial for understanding this phenomenology. Moreover, these effects are still more pronounced in the even higher temperature accretion disks thought to exist around stellar mass black hole candidates in X-ray binaries.

This paper is organized as follows. In section 2 we describe in detail our basic physical assumptions and numerical methods in treating the effects of Comptonization and metal opacities. We then describe in section 3 an approximate analytic calculation of the vertical temperature structure of an atmosphere which is subject to Comptonization. In section 4 we present our new numerical models of hot accretion disks, including a detailed comparison with our previous work and that of other authors. In section 5 we discuss these results and then we summarize our conclusions in section 6.

## 2. METHOD

The basic equations for the vertical structure were discussed in detail in Paper II, to which the reader is referred for more information. The main difference here is an inclusion of Compton scattering. Since our treatment differs somewhat from more commonly used approaches (e.g., Ross, Fabian, & Mineshige 1992; Shimura & Takahara 1993 in the context of AGN disks; or Madej 1989, 1991, 1998 in the context of model atmospheres of neutron stars and white dwarfs), we will describe it here in more detail.

### 2.1. Treatment of Compton Scattering

A general treatment of Compton scattering of (unpolarized) radiation is described in Pomraning (1973). The effects of Compton scattering are described through an appropriate frequency- and angle-dependent redistribution function that incorporates Klein-Nishina corrections and the relativistic Maxwellian velocity distribution of the electrons. In the context of stellar atmosphere modeling, this approach was used e.g. by Madej (1989; 1991, 1998; Madej & Rozanska 2000) for computing model atmospheres of neutron stars, white dwarfs, and X-ray irradiated B stars.

We are interested here in accurately treating the extreme ultraviolet/soft X-ray emission of annuli with temperatures much less than the electron rest mass energy. In this non-relativistic regime, Compton scattering can be incorporated in the radiative transfer equation through a Kompaneets-like term, i.e. by replacing the exact angle-frequency redistribution integral by a Fokker-Planck form. We present details of how this can be implemented numerically in Appendix A. For all the calculations presented in this paper, we use a Compton source function which is averaged over all angles, analogous to the standard isotropic Kompaneets equation (e.g. Rybicki & Lightman 1979). We stress, however, that we do not assume that the radiation field is isotropic. Once an atmosphere structure has converged, our treatment could be improved by performing a formal solution of the radiative transfer equation with the full angle-dependent Compton source function (see Appendix A).

We adopt the notation commonly used in stellar atmosphere modeling, i.e. we express a photon's energy through its frequency,  $\nu$ , and the photon occupation number through the specific intensity of radiation,  $I_\nu$ . Also, we often formally express a dependence on frequency through a subscript  $\nu$ . In the plane-parallel atmospheres we are considering, the radiative transfer

equation may be written as

$$\mu \frac{\partial I_\nu(\mu)}{\partial \tau_\nu} = I_\nu(\mu) - \epsilon_\nu S_\nu^{\text{th}} - \lambda_\nu \bar{S}_\nu^{\text{Compt}}. \quad (1)$$

Here  $\mu$  is the direction cosine between the photon propagation direction and the vertical. The monochromatic optical depth,  $\tau_\nu$ , is defined by

$$d\tau_\nu = -(\kappa_\nu^{\text{th}} + \sigma_\nu) dz \equiv -\chi_\nu dz, \quad (2)$$

where  $\kappa_\nu^{\text{th}}$  is the total thermal absorption coefficient at frequency  $\nu$  (including contributions from all bound-free, free-free, and possibly bound-bound transitions which operate at this frequency), and the scattering coefficient is given by

$$\sigma_\nu = n_e \sigma_T (1 - 2x). \quad (3)$$

Here  $\sigma_T$  is the Thomson cross-section, and the dimensionless frequency  $x$  is given by

$$x = \frac{h\nu}{m_e c^2}. \quad (4)$$

The  $-2x$  term in equation (3) accounts for the Klein-Nishina reduction in scattering cross-section, to first order in  $x$ .

We define the “photon destruction probability”,  $\epsilon_\nu$ , as

$$\epsilon_\nu = \frac{\kappa_\nu^{\text{th}}}{\kappa_\nu^{\text{th}} + \sigma_\nu}. \quad (5)$$

and the “scattering probability”,  $\lambda_\nu$ , as

$$\lambda_\nu = \frac{n_e \sigma_T}{\kappa_\nu^{\text{th}} + \sigma_\nu} = \frac{1 - \epsilon_\nu}{1 - 2x}. \quad (6)$$

Note that in contrast to the case of coherent scattering,  $\lambda_\nu \neq 1 - \epsilon_\nu$ . The thermal source function is given by

$$S_\nu^{\text{th}} = \frac{\eta_\nu^{\text{th}}}{\kappa_\nu^{\text{th}}}, \quad (7)$$

where  $\eta_\nu^{\text{th}}$  is the thermal emission coefficient, which contains contributions from all the spontaneous inverse processes to those giving rise to thermal absorption at frequency  $\nu$ . As is customary, we treat the stimulated emission for these processes as negative absorption.

The angle-averaged “Compton source function” is given by

$$\bar{S}_\nu^{\text{Compt}} = (1 - x)J_\nu + (x - 3\Theta)J'_\nu + \Theta J''_\nu + \frac{c^2}{2h\nu^3} J_\nu 2x(J'_\nu - J_\nu), \quad (8)$$

where

$$\Theta = \frac{kT}{m_e c^2}, \quad (9)$$

$J_\nu$  is the angle-averaged intensity, and  $J'_\nu$  and  $J''_\nu$  are defined as

$$J'_\nu = \frac{\partial J_\nu}{\partial \ln \nu} \quad \text{and} \quad J''_\nu = \frac{\partial^2 J_\nu}{\partial (\ln \nu)^2}. \quad (10)$$

A detailed derivation of equation (8) is presented in Appendix A, but we note that it is simply equivalent to taking the emission terms of the isotropic Kompaneets equation (e.g. Rybicki

& Lightman 1979), and replacing the photon occupation number with  $J_\nu/\nu^3$ . The last term on the right-hand side of equation (8) represents stimulated Compton scattering. Note that the Thomson limit of the scattering source function can be formally obtained by setting  $x = \Theta = 0$  in equation (8), in which case we obtain  $S_\nu^{\text{Compt}} = J_\nu$ , i.e., the usual Thomson scattering source function for isotropic scattering.

We write the energy balance equation in a manner very similar to equation (36) of Paper II, viz.

$$\frac{\partial F_z}{\partial z} = 4\pi \int_0^\infty \chi_\nu (S_\nu^{\text{tot}} - J_\nu) d\nu. \quad (11)$$

Here  $F_z$  is the vertical component of the energy flux. Note that in the case of coherent (Thomson) scattering, the absorption and emission contributions exactly cancel in the right hand side of equation (11), so the net radiative cooling term contains only thermal absorption and emission terms. Compton scattering, however, affects the thermal balance, so we have to retain the *total* absorption coefficient  $\chi_\nu$  and the *total* source function,  $S_\nu^{\text{tot}} \equiv \epsilon_\nu S_\nu^{\text{th}} + \lambda_\nu S_\nu^{\text{Compt}}$ .

The coupled set of structural equations (1), (11), together with the hydrostatic equilibrium and statistical equilibrium equations (given explicitly in Paper II), discretized in frequency and depth, is solved by the hybrid Complete Linearization/Accelerated Lambda Iteration (CL/ALI) method (Hubeny & Lanz 1995). The only new ingredient here, the Compton source function, is given by

$$S_i^{\text{Compt}} = A_i J_{i-1} + B_i J_i + C_i J_{i+1} + J_i (U_i J_{i-1} + V_i J_i + W_i J_{i+1}), \quad (12)$$

where  $i$  is the frequency index,  $J_i \equiv J(\nu_i)$ , and the coefficients  $A - C$  and  $U - W$  are functions of the parameters  $x$  and  $\Theta$ . They also depend on the form of the difference formula for differential operators in frequency. We use here a simple second order difference formula. Detailed expressions for the coefficients are given in Appendix A. Equation (12) is valid for the interior points of the frequency grid:  $i = 2, \dots, NF - 1$  ( $NF$  being the total number of frequency points). For boundary conditions in frequency space, we use the following procedure: (i) For the lowest frequency ( $i = 1$ ), we assume that the mean intensity follows the Planck function in the Rayleigh-Jeans limit,  $J_\nu \propto (2kT/c^2)\nu^2$  so that

$$J'_\nu = 2J_\nu, \quad J''_\nu = 4J_\nu. \quad (13)$$

(ii) Analogously, for the highest frequency ( $i = NF$ ), we assume the Wien limit,

$$J_\nu \propto \frac{2h\nu^3}{c^2} \exp(-h\nu/kT), \quad (14)$$

and thus

$$J'_\nu = (3 - z)J_\nu, \quad J''_\nu = [(3 - z)^2 - z]J_\nu, \quad (15)$$

where

$$z = h\nu/kT = x/\Theta. \quad (16)$$

The off-diagonal terms  $A_i$ ,  $C_i$ ,  $U_i$ , and  $W_i$  therefore vanish for  $i = 1$  and  $i = NF$ .

Since the boundary condition (14) is somewhat artificial, we have also tested another type of boundary condition, assuming

that the mean intensity of radiation at the highest frequency is given by a power-law,

$$J_\nu \propto \nu^{-\beta}, \quad (17)$$

in which case

$$J'_\nu = -\beta J_\nu, \quad J''_\nu = \beta^2 J_\nu. \quad (18)$$

We have found that the choice of boundary conditions only marginally influences the radiation intensity. This is because we adopt the highest frequency to be so high that the emergent flux is lower than the flux at the peak by several orders of magnitude.

The hybrid CL/ALI scheme allows for an arbitrary partitioning of “linearized” and “ALI” frequency points, i.e., those where the mean intensity of radiation is linearized, and those treated through the ALI scheme (and therefore not linearized), respectively. For all the calculations in this paper, we chose frequencies in the continuum with  $\nu > 10^{15} \text{ s}^{-1}$  to be linearized, while the rest were treated within the ALI scheme. Hence all the frequencies where Compton scattering could be important were linearized. In the future, we intend to implement an improved ALI treatment of Comptonization that will allow us to treat all frequencies as ALI frequencies, which would lead to a significant reduction of computer time. Work on this problem is in progress and will be described in a future paper.

In the linearized transfer equation, there is no problem treating the frequency coupling induced by Comptonization (i.e., the presence of the  $A_i$  and  $C_i$  terms in equation 12) or the non-linearity due to stimulated Compton scattering. However, before entering a linearization step, one must perform a “formal solution” of the transfer equation, i.e., a solution with the known, current thermal source function. This is very easy in the case of Thomson scattering because one can simply solve the transfer equation for one frequency at a time. The angular dependence of the radiation field is also easy to deal with using the Feautrier method (e.g., Mihalas 1978). The formal solution determines the variable Eddington factor,  $f_\nu \equiv K_\nu/J_\nu$ , where  $K_\nu$  is the second moment of the specific intensity:  $K_\nu = (1/2) \int_{-1}^1 I_\nu(\mu) d\mu$ .

In the case of Compton scattering, even the formal solution presents numerical complications because we cannot use the frequency-by-frequency strategy. In the present version of our computer program TLUSDISK (see also Paper II), we use the following procedure for the formal solution of the transfer equation with Comptonization. We first solve the transfer equation in the second-order form (e.g., Mihalas 1978), viz.

$$\frac{\partial^2 (f_i J_i)}{\partial \tau_i^2} = J_i - S_i^{\text{tot}}, \quad (19)$$

where we assume a current value of the Eddington factor  $f_i$ . We then discretize in depth, and organize the mean intensities  $J_{i,d}$  ( $i$  is the frequency index and  $d = 1, \dots, D$  is the depth index) in a set of column vectors

$$\mathbf{J}_i \equiv (J_{i,1}, J_{i,2}, \dots, J_{i,D})^T, \quad (20)$$

so that the mean intensity vector contains intensities at all depth points for a given frequency point  $i$ . The resulting discretized transfer equation reads

$$-\mathbf{A}_i \mathbf{J}_{i-1} + \mathbf{B}_i \mathbf{J}_i - \mathbf{C}_i \mathbf{J}_{i+1} = \mathbf{L}_i. \quad (21)$$

Here the matrices  $\mathbf{B}$  are tridiagonal (because of the difference representations of the second derivative with respect to depth), while the matrices  $\mathbf{A}$  and  $\mathbf{C}$  are diagonal (because the terms containing the frequency derivatives are local in physical space). Detailed expressions for the elements of matrices  $\mathbf{A}$ ,  $\mathbf{B}$  and  $\mathbf{C}$  are given in Appendix A. We avoid the nonlinearity due to the stimulated scattering term by writing the Compton source function as

$$S_i^{\text{Compt}} = A_i J_{i-1} + B_i J_i + C_i J_{i+1} + J_i (U_i J_{i-1}^{\text{old}} + V_i J_i^{\text{old}} + W_i J_{i+1}^{\text{old}}), \quad (22)$$

i.e., by assuming that the stimulated contribution is evaluated using the current (“old”) values of the mean intensity. If needed, the formal solution may be iterated to obtain an improved stimulated contribution, or one may devise a linearization procedure for the formal solution itself (which is distinct from our global linearization where we solve simultaneously all the structural equations). We have tested both approaches, and found that such refinements are never needed in actual model calculations.

Solution of equation (21) is done by standard Gauss-Jordan elimination, consisting of a forward elimination followed by a back-substitution, just as in the original Feautrier method for the Thomson scattering case.

Finally, the new Eddington factors are obtained by performing a set of elementary formal solutions for one frequency and angle at a time, with the total source function evaluated using the previously determined values of the mean intensity at all frequencies.

## 2.2. Treatment of Metals

We consider the following chemical species: H, He, C, N, O, Ne, Mg, Si, S, Ar, Ca, Fe, and Ni. We allow for all possible ionization stages, from neutrals to fully stripped atoms (e.g., Fe I to Fe XXVII). For the computations presented in this paper, we treat all ions except H I and He II as one-level atoms. This is done in order to explore the basic effects of metal opacities, together with Comptonization and departures from LTE, in an efficient way. We plan to use more extended model atoms in future calculations; very likely by adopting model atoms similar to those in the X-ray photoionization code XSTAR (Kallman 2000). For hydrogen, we use a 9-level model atom (where the ninth level is a merged “superlevel” of all higher states) as in Papers I-III. He II is represented as a 14-level atom. Since we consider only hot disks here, He I is represented by a 1-level atom, in contrast to Papers I-III where it was represented by a 14-level atom. We tested that this approximation does not lead to any errors since He I has negligible abundance in the current models.

For hydrogenic ions, we use the standard analytic expression for the photoionization cross-section. For all nonhydrogenic metal ion photoionization cross-sections, we use data from XSTAR, version 1, kindly supplied by Tim Kallman (subroutine `bkhsgo`, based on data from Barfield, Koontz, & Huebner 1972). XSTAR was recently upgraded to version 2, and now uses more recent sources of photoionization cross-sections (the Opacity Project and others); we also plan to adopt these cross-sections in future calculations.

We take into account all inner-shell photoionization processes, but make the simplifying assumption that if an Auger electron is energetically possible, then it is in fact produced and the photoionization results in a jump by two stages of ionization to a ground state configuration. We therefore neglect both

fluorescence and multiple Auger electron ejection arising from inner shell photoionization. Note that this is not a good approximation for low ionization stages of metals, where multiple Auger electron ejection is likely after an inner shell photoionization (e.g. Kaastra & Mewe 1993). This might be important in regions where non-LTE effects are important in determining the abundance of these ion species. In future calculations we will lift these simplifying assumptions and consider more elaborate inner shell photoionization branching possibilities.

We include the effects of collisional ionization of the outermost valence shell electron of each metal ion species by again using data from XSTAR, version 1 (subroutine `cion`). Once again, we plan on improving this treatment with more modern data in the future.

Dielectronic recombination is handled using the subroutine `direc` from XSTAR, version 1. This is based on data from Aldrovandi & Pequignot (1973), Nussbaumer & Storey (1983), and Arnaud & Raymond (1992). Numerically, we treat dielectronic recombination by introducing an artificial modification of the photo-ionization cross-section, which has the advantage that the detailed balance relations are automatically satisfied. We describe this procedure in more detail in Appendix B.

## 3. UNDERSTANDING TEMPERATURE STRUCTURE IN THE PRESENCE OF COMPTONIZATION

Before we turn to actual numerical results, it is worthwhile developing a simple analytic model that will allow us to understand the vertical temperature profile in the presence of Compton scattering. A similar study for the case of “classical” disks without Comptonization was done by Hubeny (1990). The approach developed here is its generalization. We note that Madej (1989) considered a similar LTE-gray model in the context of neutron star atmospheres (i.e., with no viscous heating), although he only provided a numerical solution.

### 3.1. Energy Balance

The energy balance equation may be written in the form (see Paper II)

$$\frac{dF_{\text{rad}}}{dm} = -\sigma T_{\text{eff}}^4 \frac{w(m)}{m_0 \bar{w}}. \quad (23)$$

Here  $w(m)$  is the dissipation rate at column density  $m$  and  $\bar{w}$  is the vertical mean of  $w$ . In evaluating  $w$  we employ the relativistic corrections of Riffert & Herold (1995) as in Paper II; replacing them with the forms advocated by Abramowicz et al. (1997) produces no significant change in the emergent spectrum.

The important point is that we can express the gradient of the radiation flux through the transfer equation

$$\frac{dF_{\text{rad}}}{dm} = 4\pi \int_0^\infty \chi_\nu (S_\nu^{\text{tot}} - J_\nu) d\nu. \quad (24)$$

Equating now the right-hand sides of equations (23) and (24) gives another form of the energy balance equation, which expresses the fact that the total energy generated locally is balanced by the net local radiative loss.

The integrand of the radiative loss term is given by

$$\chi_\nu (S_\nu^{\text{tot}} - J_\nu) = \kappa_\nu (S_\nu^{\text{th}} - J_\nu) + n_e \sigma_T \left[ x J_\nu + (x - 3\Theta) J'_\nu + \Theta J''_\nu + \frac{c^2}{2h\nu^3} J_\nu 2x (J'_\nu - J_\nu) \right]. \quad (25)$$

In the following, we neglect the stimulated scattering term, and assume that the thermal source function is given by the Planck function. We stress that this is done in this section only for developing a simple analytic model; in actual calculations these simplifications are not made. The integral in Eq. (24) can be evaluated using integration by parts for the derivative terms. After some algebra we obtain

$$\kappa_B B - \kappa_J J + \kappa_\sigma (4\Theta - \bar{x})J = \frac{\sigma}{4\pi} T_{\text{eff}}^4 \frac{w(m)}{m_0 \bar{w}}, \quad (26)$$

where  $J = \int_0^\infty J_\nu d\nu$ , and analogously for  $B$ . The mean opacities are defined by

$$\kappa_J = \int_0^\infty (\kappa_\nu^{\text{th}}/\rho) J_\nu d\nu / J, \quad (27)$$

$$\kappa_B = \int_0^\infty (\kappa_\nu^{\text{th}}/\rho) B_\nu d\nu / B, \quad (28)$$

(which is called the Planck-mean opacity), and

$$\kappa_\sigma = n_e \sigma_T / \rho. \quad (29)$$

Finally,  $\bar{x}$  is defined by

$$\bar{x} = \frac{h}{mc^2} \bar{\nu} = \frac{h}{mc^2} \frac{\int_0^\infty \nu J_\nu d\nu}{J}, \quad (30)$$

which has the meaning of a mean frequency weighted by the local mean intensity. Since the mean intensity is typically a sharply-peaked function of frequency,  $\bar{\nu}$  is close to the frequency where  $J_\nu$  attains its maximum value. We note that the traditional *Compton temperature*,  $T_C$ , is defined (e.g., Krolik 1999) as the temperature for which the term  $4\Theta - \bar{x}$  vanishes, i.e.

$$T_C = \frac{h\bar{\nu}}{4k} \approx 1.2 \times 10^{-11} \bar{\nu}. \quad (31)$$

Equation (26) has a simple physical interpretation. The right-hand side expresses the net energy generated per unit mass at a given depth in the disk. The left-hand side expresses the net energy loss, i.e. the energy that has been transferred from material particles to photons. The term  $\kappa_B B - \kappa_J J$  expresses the transfer of energy from particles to photons by *thermal processes* (i.e. bound-bound, bound-free, and free-free atomic processes), while the term  $\kappa_\sigma (4\Theta - \bar{x})J$  expresses the net loss of energy of particles, in this case electrons, by Compton scattering. The latter term is in fact a generalization of the usual formula (e.g., Rybicki & Lightman 1979) for the net photon energy gain (i.e., net electron energy loss) in a single scattering, which in our notation reads

$$\frac{\Delta(h\nu)}{h\nu} = 4\Theta - x. \quad (32)$$

We also note that the ratio  $\kappa_B/\kappa_\sigma$  can be expressed as

$$\kappa_B/\kappa_\sigma = \int_0^\infty (\kappa_\nu^{\text{th}}/(n_e \sigma_T)) B_\nu d\nu / B \approx \int_0^\infty \epsilon_\nu B_\nu d\nu / B \equiv \bar{\epsilon}, \quad (33)$$

i.e. the ratio of the Planck-mean to the scattering opacity has the meaning of a *mean photon destruction parameter*. Notice that the last approximate equality only holds in the case of dominant electron scattering,  $\epsilon_\nu \ll 1$ .

To proceed further, we need an expression for the local integrated mean intensity,  $J$ . This can be obtained from the second moment of the radiative transfer equation

$$\frac{dK_\nu}{dm} = \frac{\chi_\nu}{\rho} H_\nu, \quad (34)$$

where  $H_\nu = (1/2) \int_{-1}^1 I_\nu(\mu) d\mu$  is the first moment of the specific intensity. We now invoke the Eddington approximation, i.e.,  $K_\nu = J_\nu/3$ , and integrate equation (34) over all frequencies. We obtain, again in the case of dominant electron scattering,

$$\frac{dJ}{dm} \approx 3\kappa_\sigma H = \frac{3\kappa_\sigma}{4\pi} F_{\text{rad}}. \quad (35)$$

The local radiation flux follows from integrating equation (23), viz.

$$F_{\text{rad}}(m) = \sigma T_{\text{eff}}^4 \left[ 1 - \frac{\int_0^m w(m') dm'}{m_0 \bar{w}} \right]. \quad (36)$$

Substituting equation (36) into (35) and solving it for  $J$  we obtain

$$J(m) = \frac{3\sigma}{4\pi} T_{\text{eff}}^4 \left( \frac{1}{\sqrt{3}} + \tau - \tau_w \right), \quad (37)$$

where we used the Eddington approximation form of the boundary condition,  $J(0) = H(0)\sqrt{3}$ , and expressed  $H(0)$  through the effective temperature. The optical depth is defined by

$$\tau = \int_0^m \kappa_\sigma dm' \approx \kappa_\sigma m \quad (38)$$

since we assume that hydrogen and helium are completely ionized so that  $\kappa_\sigma$  is nearly constant. This optical depth is thus the Thomson optical depth. The other optical depth in equation (37) may be called the “viscosity-weighted” optical depth, and is defined by

$$\tau_w = \int_0^m dm' \kappa_\sigma \int_0^{m'} w(m'') dm'' / m_0 \bar{w}. \quad (39)$$

In the case of a depth-independent kinematic viscosity,

$$\tau_w = \frac{\tau^2}{2\tau_{\text{tot}}} \quad (40)$$

where  $\tau_{\text{tot}} \equiv \kappa_\sigma m_0$  is the Thomson optical depth at the mid-plane.

Finally, combining equations (26) and (37), we arrive at the basic equation of this section,

$$\kappa_B \left( \frac{T}{T_{\text{eff}}} \right)^4 = \frac{3}{4} \left( \frac{1}{\sqrt{3}} + \tau - \tau_w \right) [\kappa_J - \kappa_\sigma (4\Theta - \bar{x})] + \frac{w(m)}{4\bar{w}m_0}, \quad (41)$$

where we used the well-known expression  $B = (\sigma/\pi)T^4$ .

Using equation (33), and assuming, as usual, that  $\kappa_J = \kappa_B$ , we rewrite equation (41) in a more instructive form,

$$\bar{\epsilon} \left( \frac{T}{T_{\text{eff}}} \right)^4 = \frac{3}{4} \left( \frac{1}{\sqrt{3}} + \tau - \tau_w \right) (\bar{\epsilon} - 4\Theta + \bar{x}) + \frac{w(m)}{\bar{w}} \frac{1}{4\tau_{\text{tot}}}. \quad (42)$$

We see that the effects of Compton scattering are negligible if  $|4\Theta - \bar{x}| \ll \bar{\epsilon}$ , in which case we recover equation 3.11 of Hubeny (1990).

Before we discuss the meaning and implications of equation (42) in more detail, we first turn to estimating the mean frequency.

### 3.2. The Mean Frequency

A determination of the mean frequency is easy if the mean intensity is proportional to the Planck function,  $J_\nu = aB_\nu$ , where  $a$  is a frequency-independent constant. In this case

$$\bar{\nu} = \frac{\int_0^\infty \nu^4 / [\exp(h\nu/kT) - 1] d\nu}{\int_0^\infty \nu^3 / [\exp(h\nu/kT) - 1] d\nu} = \frac{kT}{h} \frac{\Gamma(5)}{\Gamma(4)} \frac{\zeta(5)}{\zeta(4)} \approx 3.83 \frac{kT}{h}. \quad (43)$$

Here,  $\Gamma$  is the Euler gamma function and  $\zeta$  is the Riemann zeta function (e.g., Abramowitz & Stegun 1970). The Compton cooling term is thus given by

$$4\Theta - \bar{x} = \Theta(4 - 3.83) = 0.17\Theta = 2.867 \times 10^{-11} T. \quad (44)$$

Deep in the atmosphere,  $J_\nu \approx B_\nu(T)$ , where  $T$  is the local temperature. Therefore, the Compton cooling term is *positive*, and is determined by the *local* temperature.

At the surface, the mean frequency can be estimated as follows. Let us assume for simplicity that the total Thomson optical depth is large. Then the surface mean intensity, assuming the Eddington approximation, is given by (see, e.g., Mihalas 1978 or Rybicki & Lightman 1979)

$$J_\nu(\tau = 0) \approx \sqrt{\epsilon_\nu} B_\nu(T(\tau = 1/\sqrt{3\epsilon_\nu})). \quad (45)$$

In other words, the mean intensity is still proportional to the Planck function; however the constant of proportionality,  $\sqrt{\epsilon_\nu}$ , depends on frequency, and the temperature at which the Planck function is evaluated is *not* the local temperature, but the temperature at depth  $\tau = \tau_\nu^{\text{form}} = 1/\sqrt{3\epsilon_\nu}$ , which may actually be quite large. We call the depth  $\tau_\nu^{\text{form}}$  the *effective depth of formation*. We note that there is an intimate relation between the effective depth of formation and the traditional *effective optical depth* (e.g., Rybicki & Lightman 1979; their equation 1.98). The effective optical depth is given by (in our notation)

$$\tau_\nu^* \approx \sqrt{\tau_\nu^{\text{th}} \tau_\nu} \approx \tau_\nu \sqrt{\epsilon_\nu}. \quad (46)$$

Our effective depth of formation is thus equal, up to a factor of the order of unity, to the optical depth of the point where the effective optical depth is equal to unity, i.e.,  $\tau_\nu^* \approx 1$  at  $\tau_\nu \approx 1/\sqrt{\epsilon_\nu}$ . In view of all the approximations made in deriving Eq. (45) (the Eddington approximation, a depth-independent  $\epsilon_\nu$ , etc.), the factor  $\sqrt{3}$  is inconsequential.

To proceed further, let us assume that in the deep layers we have  $4\Theta - \bar{x} = 2.867 \times 10^{-11} T < \bar{\epsilon}$ , and thus the Compton term can be neglected. This is actually a reasonable approximation for estimating the surface value of  $\bar{\nu}$  for our disks, since typical local temperatures are of the order of a few times  $10^6$  K, while  $\bar{\epsilon} \approx 10^{-4}$  in the deep layers (note that in the deep layers  $\epsilon$  is larger than near the surface because of the higher density). Assuming also  $\tau_{\text{tot}} \gg 1$ , we are left with a rough estimate of the temperature in the deep layers,  $T^4(\tau) \approx (3/4)T_{\text{eff}}^4 \tau$ , which follows from equation (41), neglecting here for simplicity a correction term of the order of unity coming from  $\tau_w$ .

We denote the temperature at which the Planck function in equation (45) is evaluated as  $T^*$ ; it is thus given by

$$T^* = (3/4)^{1/4} T_{\text{eff}} 3^{-1/8} \epsilon_\nu^{-1/8}. \quad (47)$$

The dependence of  $T^*$  on frequency arises only through the term  $\epsilon_\nu^{-1/8}$ , and is therefore rather weak. We may then replace

$\epsilon_\nu^{-1/8}$  by  $(\bar{\epsilon})^{-1/8}$ . Similarly, if we assume that  $\sqrt{\epsilon_\nu}$  varies with frequency much more slowly than  $B_\nu$  (at least around the maximum of the Planck function that contributes most to the integrals), then we may again use equation (43) to obtain

$$\begin{aligned} \bar{\nu} &= 3.83 (kT^*/h) = 3.83 (k/h) (3/4)^{1/4} 3^{-1/8} (\bar{\epsilon})^{-1/8} T_{\text{eff}} \\ &\approx 6.5 \times 10^{10} (\bar{\epsilon})^{-1/8} T_{\text{eff}}. \end{aligned} \quad (48)$$

The Compton cooling term may thus be expressed as

$$4\Theta - \bar{x} = \frac{k}{m_e c^2} (4T - 3.83 T^*) = 6.75 \times 10^{-10} (T - 0.96 T^*), \quad (49)$$

where we left the “formation temperature”,  $T^*$ , unspecified. This equation is instructive because we easily see that if  $T > 0.96 T^*$ , Compton scattering leads to cooling of the surface layers, while if  $T < 0.96 T^*$ , Compton scattering heats the layers. If Compton scattering is the dominant source of opacity and emissivity, then the surface layers have the temperature  $T \approx T^*$ .

### 3.3. Surface temperature

An estimate of the surface temperature is of considerable interest since it will show whether our models are in principle able to produce high-temperature external layers, traditionally called disk *coronae*.

Using the results of the previous section, we can rewrite equation (42) at the surface (i.e.  $\tau = \tau_w = 0$ ) as

$$\bar{\epsilon} \left( \frac{T_0}{T_{\text{eff}}} \right)^4 = \frac{\sqrt{3}}{4} \left[ \bar{\epsilon} - \frac{4k}{m_e c^2} (T_0 - 0.96 T^*) \right] + \frac{w(0)}{\bar{w}} \frac{1}{4\tau_{\text{tot}}}. \quad (50)$$

Using equation (47), and introducing a normalized surface temperature,  $t \equiv T_0/T_{\text{eff}}$ , we obtain the following fourth-order algebraic equation for  $t$ ,

$$at^4 + bt = c, \quad (51)$$

where

$$a = \bar{\epsilon}, \quad b = 2.92 \times 10^{-10} T_{\text{eff}}, \quad (52)$$

and

$$c = 0.43 \bar{\epsilon} + 2.92 \times 10^{-10} T_{\text{eff}} (\bar{\epsilon})^{-1/8} + \frac{w(0)}{\bar{w}} \frac{1}{4\tau_{\text{tot}}}. \quad (53)$$

A general solution of equation (51) is possible to find analytically, but is quite cumbersome. However, we may consider several limiting cases:

1)  $a \gg b$ , i.e.  $\bar{\epsilon} \gg 3 \times 10^{-10} T_{\text{eff}}$

This is the limit of negligible Compton scattering, which applies if either the mean photon destruction parameter  $\bar{\epsilon}$  is very large, or the effective temperature is very low. In this case the solution of equation (51) is simply  $t = (c/a)^{1/4}$ , i.e.

$$\frac{T_0}{T_{\text{eff}}} \approx \left( 0.43 + \frac{w(0)}{\bar{w}} \frac{1}{4\tau_{\text{tot}}} \frac{1}{\bar{\epsilon}} \right)^{1/4}. \quad (54)$$

There are two limiting cases in this situation. If the second term in the brackets is negligible, then one is left with the classical stellar-atmosphere surface temperature:  $T_0 \approx 0.81 T_{\text{eff}}$ . The second term is important, if (i)  $w(0)/\bar{w}$  is large, i.e., if the viscosity increases towards the surface; or (ii) if the term  $\bar{\epsilon}\tau_{\text{tot}}$  is small. Note that the latter term is in fact the total Planck-mean optical depth, i.e. the total optical depth for pure thermal

absorption. Therefore, the surface temperature may be large (i.e., larger than  $T_{\text{eff}}$ ) even in the absence of Compton scattering and an outward-increasing dissipation. This is readily explained. Thomson scattering does not influence the energy balance. Since we now have an optically thin disk with respect to the total Planck-mean opacity, the total energy radiated away is proportional to  $S\tau$ , where  $S$  is the source function, and  $\tau$  the total optical depth. We take  $S = B \propto T^4$ , while the total energy dissipated is proportional to  $T_{\text{eff}}^4$ . These energies are equal, so that we obtain  $(T/T_{\text{eff}})^4 \propto 1/\tau$ . In other words, an effectively thin slab must be hotter than a thicker slab to be able to radiate the same dissipated energy.

2)  $a \ll b$ , i.e.  $\bar{\epsilon} \ll 3 \times 10^{-10} T_{\text{eff}}$ .

This is the limit of dominant Compton scattering. The solution of equation (51) is  $t = c/b$ , i.e.

$$\frac{T_0}{T_{\text{eff}}} \approx (\bar{\epsilon})^{-1/8} + \frac{w(0)}{\bar{w}} \frac{1}{4\tau_{\text{tot}}} \frac{1}{2.92 \times 10^{-10} T_{\text{eff}}}, \quad (55)$$

provided that  $at^4$  is also  $\ll bt$ , i.e.,  $t \ll (b/a)^{1/3}$ . When this criterion is satisfied, there are two limiting cases. If the second term on the right-hand side is small, then  $T_0 \approx (\bar{\epsilon})^{-1/8} T_{\text{eff}}$ . For typical values of  $\bar{\epsilon}$  of the order of  $10^{-6}$  to  $10^{-5}$ , we see that Compton scattering leads to a heating of the surface layers up to a factor of 3 – 6 above the effective temperature! Obviously, the surface temperature is larger for smaller values of  $\bar{\epsilon}$  because Compton scattering becomes more efficient with respect to the thermal processes. On the other hand, if the second term is important, either because  $w(0)/\bar{w}$  is large or the total optical depth is small, then the solution is given by the second term of equation (55). When  $at^4$  is not small compared to  $bt$ , equation (54) is again roughly correct.

We summarize the behavior of the surface temperature in Figures 1 and 2.

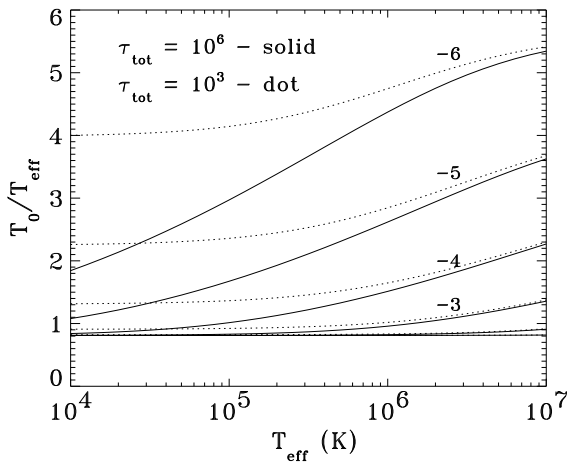


FIG. 1— Approximate surface temperature, expressed as  $T_0/T_{\text{eff}}$ , displayed as a function of  $T_{\text{eff}}$ , for different values of  $\bar{\epsilon}$ , and for two values of  $\tau_{\text{tot}}$ . The individual curves are labeled by the value of  $\log \bar{\epsilon}$ . Solid lines are for a total optical depth  $\tau_{\text{tot}} = 10^6$ , and dotted lines are for  $\tau_{\text{tot}} = 10^3$ .

For simplicity, we assume constant viscosity, i.e.  $w(0)/\bar{w} = 1$ ; we will study the effects of an increasing viscous dissipation towards the surface in a subsequent paper. Figure 1 displays the surface temperature, expressed as  $T_0/T_{\text{eff}}$  as a function of  $T_{\text{eff}}$ , for different values of  $\bar{\epsilon}$ , and for two values of  $\tau_{\text{tot}}$ . Figure 2 displays the surface temperature as a function of the total optical depth, for several values of  $\bar{\epsilon}$  and  $T_{\text{eff}}$ .

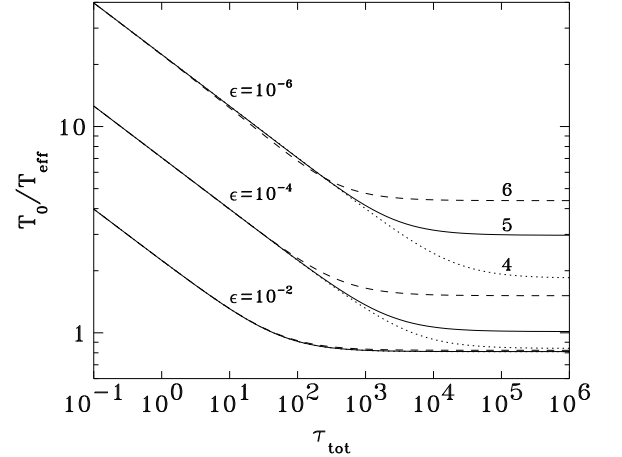


FIG. 2— Approximate surface temperature, expressed as  $T_0/T_{\text{eff}}$ , displayed as a function of  $\tau_{\text{tot}}$ , for different values of  $\bar{\epsilon}$ , and for three values of  $T_{\text{eff}}$ . The individual curves are labeled by the value of  $\bar{\epsilon}$  and by the value of  $\log T_{\text{eff}}$ . Solid lines have  $T_{\text{eff}} = 10^5$  K, dotted lines have  $T_{\text{eff}} = 10^4$  K, and dashed lines have  $T_{\text{eff}} = 10^6$  K.

We now turn to the accurate numerical models, and show that the above estimates agree reasonably well with exact numerical results.

## 4. RESULTS

### 4.1. Comparison to the models from Paper III

We shall first present a comparison of models computed with and without Comptonization. We take the hottest disk from our grid of Paper III, where the effects of Comptonization are expected to be the largest. This is a disk around a black hole with  $M = (1/8) \times 10^9 M_{\odot}$  and mass accretion rate  $\dot{M} = 1/4 M_{\odot}/\text{yr}$  (i.e. with luminosity  $L \approx 0.3 L_{\text{Edd}}$ ). To isolate the effects of Comptonization, we assume, in agreement with Paper III, that the disk consists of hydrogen and helium only. Also following Paper III, we take the local viscosity to be described by a two-step power law, with a constant kinematic viscosity in the inner 99% of the disk mass, while the viscosity is assumed to decrease as  $m^{-2/3}$  in the outermost 1% of the mass (see Paper III for details). The reason we chose an artificial decrease of viscosity with height was to prevent a “thermal catastrophe” of the disk in the low optical depth regions (e.g., Shaviv & Wehrse 1986). In the case of H-He models without Comptonization, there are no efficient mechanisms that are able to radiate the dissipated energy away when the atmosphere becomes optically thin in the most opaque transition; the atmosphere thus undergoes a thermal runaway. This is obviously prevented when one considers Compton instead of Thomson electron scattering, as we have shown analytically in the previous section, and will demonstrate numerically in this and subsequent sections. We show the models with vertically decreasing dissipation only for the purpose of direct comparison of the present results to those of Paper III.

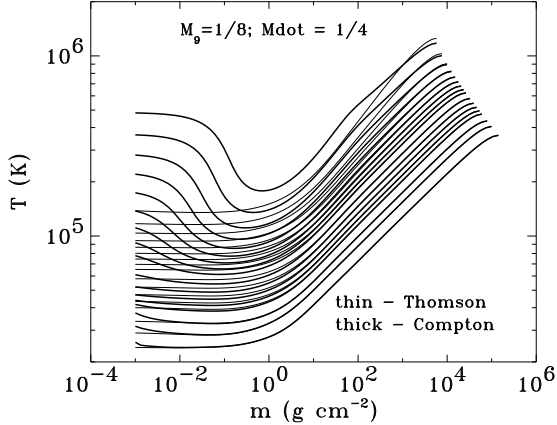


FIG. 3— Temperature as a function of depth for selected annuli. From top to bottom, the curves correspond to radii  $R/R_g = 2, 3, 4, 5, 6, 7, 8, 9, 10, 12, 14, 16, 18, 20, 25, 30, 40, 50, 60, 70, 80,$  and  $90$ . Thin lines represent the models from Paper III computed without Comptonization, while thick lines correspond to models with Comptonization.

Figure 3 displays the local electron temperature as a function of position for selected annuli. The position is expressed as column mass,  $m$ , above a given depth. The models with Comptonization exhibit a temperature rise at the surface, even for the case of viscosity decreasing outward. This is easily explained by the considerations presented in the previous section. The hottest annuli have  $T_{\text{eff}} \approx 2 \times 10^5$  K. The typical value of  $\bar{\epsilon}$  is about  $10^{-5}$ , so that  $\epsilon < 3 \times 10^{-10} T_{\text{eff}} \approx 6 \times 10^{-5}$ , and thus we are in the regime of important Compton scattering, where Eq. (55) applies. Since viscosity is forced to decrease outward, the second term on the right-hand side of Eq. (55) is negligible, and we therefore find  $T/T_{\text{eff}} \approx 2$ , which is indeed seen in Figure 3. The cooler annuli have progressively larger values of  $\bar{\epsilon}$  and lower  $T_{\text{eff}}$ , and therefore are less and less influenced by Comptonization. Again, this is nicely verified by numerical calculations.

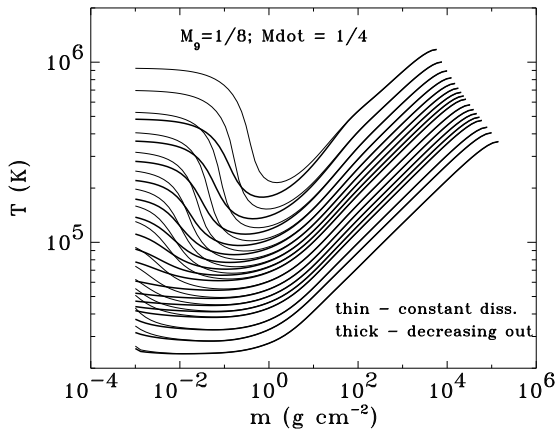


FIG. 4— Temperature as a function of depth for selected individual annuli. The curves correspond to radii  $R/R_g$  (from top to bottom)  $2, 3, 4, 5, 6, 7, 8, 9, 10, 12, 14, 16, 18, 20, 25, 30, 40, 50, 60, 70, 80,$  and  $90$ . Thin lines represent the models with constant dissipation, while thick lines represent the models with decreasing dissipation towards the surface.

To see the effect of changing the dissipation law on the temperature structure, we have computed the same models as

above, but keeping the kinematic viscosity constant with depth, i.e. without an artificial decrease of viscosity at the surface. The temperature structure for the individual annuli is displayed in Figure 4. Note that models with constant dissipation were impossible to construct with the original assumption of Thomson scattering, because the temperature exhibited a runaway instability behavior. The behavior of the surface temperature is again easily explained using Eq. (55). In this case, we have  $w(0)/\bar{w} = 1$ . Moreover, for the hottest annuli we have  $T_{\text{eff}} \approx 2 \times 10^5$  K, and  $\tau_{\text{tot}} \approx 2 \times 10^3$ , so the second term in equation (55) is about 2. Since the first term is also roughly equal to 2, we see that in this particular case the Compton heating and the viscous heating have a comparable effect on the surface temperature. The resulting  $T/T_{\text{eff}}$  should be around 4, which is again nicely verified by numerical calculations.

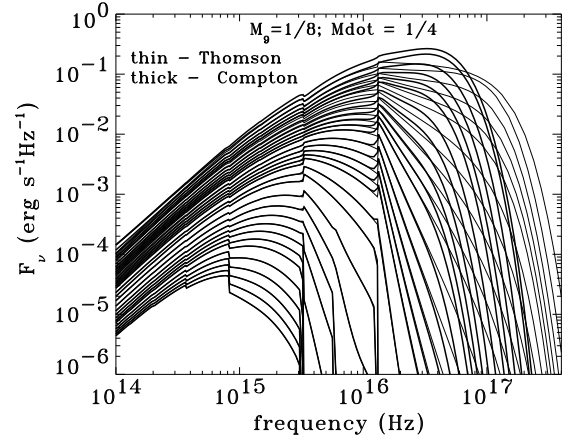


FIG. 5— Local emergent flux for the individual annuli. From top to bottom, the curves correspond to radii  $R/R_g = 1.5, 2, 2.5, 3, 3.5, 4, 5, 6, 7, 8, 9, 10, 12, 14, 16, 18, 20, 25, 30, 40, 50, 60, 70, 80, 90, 100, 120, 140, 160, 180,$  and  $200$ . Thin lines represent the models from Paper III computed without Comptonization, and thick lines represent the models with Comptonization.

From a practical point of view, the most important feature is the behavior of the emergent flux from the individual annuli when Comptonization is taken into account. Figure 5 displays a comparison between the model without (thin lines) and with (heavy lines) Comptonization for the individual annuli displayed in previous figures.

The models with constant and with decreasing kinematic viscosity at the surface are indistinguishable in the plot. This is because only the surface layers are influenced by changes in the dissipation law, while the emergent continuum radiation is formed in much deeper layers. The emergent flux would be influenced if the dissipation increases outward, in which case a hot corona (with temperatures of the order  $10^8$  to  $10^9$  K) is formed. Such a corona would produce a significantly increased X-ray flux. We will present a more extended study of this phenomenon in the next paper of this series.

Comptonization in hot annuli leads to the well-known increase of the flux in the EUV and the soft X-ray region ( $\nu < 10^{17}$  s $^{-1}$ ). For larger frequencies, the flux drops fast, so that the flux for the Comptonized model is lower than the flux for the original, Thomson-scattering, model. An analogous behavior was also found for the emergent spectra of (hotter and denser) neutron star atmospheres (Madej 1991). This behavior is readily explained by examining the net photon energy gain (or loss) as a function of frequency. As discussed in Section 3 (see also



Rybicki & Lightman 1979), the net energy gain of a photon with frequency  $\nu$  is given by  $4\Theta - x$ . Since we are dealing with a depth-dependent situation, one has to evaluate the appropriate  $\Theta$  at the effective depth of formation,  $\tau_\nu \approx \tau_\nu^{\text{form}} \approx 1/\sqrt{\epsilon_\nu}$ . Note that when  $\tau_\nu^{\text{form}} > \tau_{\text{tot}}$ , where  $\tau_{\text{tot}}$  is the optical depth at the midplane (generally, it is a frequency-dependent quantity, but the dependence is very weak in the case of dominant electron scattering), the disk is *effectively thin*. The effective depth of formation should thus be more generally given by  $\tau_\nu^{\text{form}} \approx \min(1/\sqrt{\epsilon_\nu}, \tau_{\text{tot}})$ . Nevertheless, we will assume an effectively thick disk in the following discussion. The temperature at the formation depth is thus given by [see also Eq. (47)],  $T_\nu^* \approx T_{\text{eff}} \epsilon_\nu^{-1/8}$ .

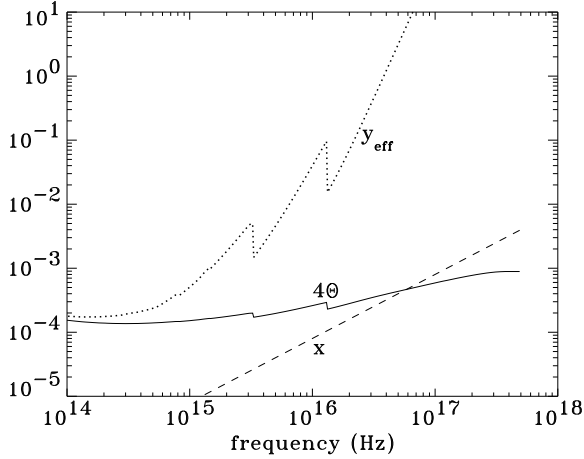


FIG. 6— Computed value of  $4\Theta(T_\nu^*)$  compared to  $x$  as a function of frequency. The Compton parameter  $y_{\text{eff}}$  is also displayed. All the quantities are dimensionless numbers.

In Figure 6 we display the computed value of  $4\Theta(T_\nu^*)$  compared to  $x$  as a function of frequency. We see that for  $\nu \lesssim 6 \times 10^{16}$ , the term  $4\Theta - x$  is positive, and therefore Comptonization leads to a net *increase* in photon frequency, while for  $\nu \gtrsim 6 \times 10^{16}$  the photon frequency is *decreased* by Comptonization. These values tell us how the photon frequency is shifted, but do not tell us about the number of available scatterings and thus about the resulting effects of the photon frequency shifts on the emergent spectrum. In order to verify that Comptonization in fact has a significant effect on the spectrum, we also show the effective Compton parameter  $y_{\text{eff}}$ , which is defined by (Rybicki & Lightman 1979)

$$y_{\text{eff}} = 4\Theta \max[\tau_\nu^{\text{form}}, (\tau_\nu^{\text{form}})^2]. \quad (56)$$

Here the factor  $\max[\tau_\nu^{\text{form}}, (\tau_\nu^{\text{form}})^2]$  expresses the total number of scatterings of a photon with frequency  $\nu$ . Since in our case  $\tau_\nu^{\text{form}} \approx 1/\sqrt{\epsilon_\nu}$  and thus  $\tau_\nu^{\text{form}} \gg 1$ , we have

$$y_{\text{eff}} \approx 4 \times 10^{-10} T_{\text{eff}} \epsilon_\nu^{-9/8}. \quad (57)$$

We can roughly estimate  $\epsilon_\nu$  and therefore  $y_{\text{eff}}$  as follows. Let us assume for simplicity a relatively hot plasma where all hydrogen and helium are almost completely ionized, and that the only sources of thermal opacity are the Lyman continua and the free-free transitions of hydrogen and ionized helium. The bound-free and free-free opacities are thus given by (see, e.g., Mihalas 1978)

$$\kappa_{\text{bf}}(\nu) \approx 1.17 \times 10^{14} T^{-3/2} n_e \nu^{-3}$$

$$\left[ n_p e^{0.158/T_6} H(\nu, \nu_H) + Z^4 n_{\text{HeIII}} e^{0.631/T_6} H(\nu, Z^2 \nu_H) \right], \quad (58)$$

and

$$\kappa_{\text{ff}}(\nu) \approx 3.69 \times 10^8 T^{-1/2} n_e \nu^{-3} [n_p + Z^2 n_{\text{HeIII}}], \quad (59)$$

where  $Z = 2$  is the effective charge of the ionized helium;  $n_p$  and  $n_{\text{HeIII}}$  are the number density of protons and of helium nuclei, respectively; and  $T_6 \equiv T/10^6$ . Here we assume LTE for the hydrogen and ionized helium ground-state populations. We also assume that the bound-free and free-free Gaunt factors are equal to unity.  $H(\nu, \nu_0)$  is the unit step function, defined in such a way that  $H = 0$  for  $\nu < \nu_0$ , and  $H = 1$  for  $\nu \geq \nu_0$ ;  $\nu_H = 3.29 \times 10^{15} \text{ s}^{-1}$  is the frequency of the hydrogen Lyman edge. Since we assume almost completely ionized plasma, then from the charge conservation equation we obtain  $n_p = n_e/(1 + 2Y)$  and  $n_{\text{HeIII}} = n_e Y/(1 + 2Y)$ . Substituting these values, and assuming the solar abundance of helium,  $Y = 0.1$ , we obtain for  $\epsilon_\nu$

$$\epsilon_\nu \approx \frac{\kappa_{\text{bf}}(\nu) + \kappa_{\text{ff}}(\nu)}{n_e \sigma_T} \approx 6.5 \times 10^{-5} n_{14} T_6^{-1/2} \nu_{16}^{-3} \gamma_\nu(T), \quad (60)$$

where  $n_{14} = n_e/10^{14}$ ,  $\nu_{16} = \nu/10^{16}$ , and  $\gamma$  is a function of order of unity that depends only weakly on  $T$  and  $\nu$  (at least in the temperature range  $T \lesssim 2 \times 10^5 \text{ K}$  relevant here).

$$\gamma_\nu(T) = 1 + \frac{0.226}{T_6} \left[ e^{0.158/T_6} H(\nu, \nu_H) + 1.6 e^{0.631/T_6} H(\nu, 4\nu_H) \right]. \quad (61)$$

Equation (60) is valid for any temperature and electron density. We may also specify the corresponding  $\epsilon$  at the effective depth of formation,  $\epsilon_\nu^* \equiv \epsilon_\nu(T_\nu^*)$ , where  $T_\nu^*$  is given by  $T_\nu^* \approx T_{\text{eff}} (\epsilon_\nu^*)^{-1/8}$ . Substituting for  $\epsilon$  from equation (60), we obtain

$$T_{\nu,6}^* \approx 3.6 T_{\text{eff},6}^{16/15} n_{14}^{-2/15} \nu_{16}^{2/5}, \quad (62)$$

[notice that the scaling  $\Theta(T_\nu^*) \propto \nu^{2/5}$  is nicely seen in Figure 6], and thus

$$\epsilon_\nu^* \approx 3.2 \times 10^{-5} T_{\text{eff},6}^{-8/15} n_{14}^{16/15} \nu_{16}^{-16/5}. \quad (63)$$

Here we use the same notations as before, namely  $T_{\text{eff},6} \equiv T_{\text{eff}}/10^6$ , and  $T_{\nu,6}^* \equiv T_\nu^*/10^6$ . Finally, from equation (57) we have

$$y_{\text{eff}} \approx 44 T_{\text{eff},6}^{24/15} n_{14}^{-18/15} \nu_{16}^{18/5}. \quad (64)$$

Again, the approximate scaling  $y_{\text{eff}} \propto \nu^{18/5}$  is verified in Figure 6.

We see from Figure 6 that  $y_{\text{eff}} \gtrsim 1$  for  $\nu \gtrsim 3 \times 10^{16}$ , and thus Comptonization should significantly influence the emergent spectral energy distribution for these frequencies. From Figure 6 we deduce that the emergent flux for frequencies  $3 \times 10^{16} \lesssim \nu \lesssim 6 \times 10^{16}$  should be enhanced over the model with Thomson scattering only, while the opposite should apply for higher frequencies, which is indeed demonstrated by the exact results shown in Figure 5. In fact, the enhancement of flux caused by Compton scattering is seen already for lower frequencies, which is a consequence of the higher temperature for the Comptonized model (cf. Figure 3).

An inspection of Figure 5 shows that the emergent flux is influenced only for the hottest annuli, those with effective temperature above 150,000 K; the cooler annuli are influenced only

marginally. This is easily seen from equation (64). The effective temperature varies with radial coordinate roughly as  $T_{\text{eff}} \propto R^{-3/4}$ , so that  $T_{\text{eff}}^{24/15} \propto R^{-6/5}$ . Estimating the appropriate electron density is much more complex. We consider two limits. In completely radiation-pressure dominated disks, and neglecting relativistic corrections, we may consider the mass density at the effective depth of formation to be equal to the vertically averaged mass density,  $\rho_0$ . Thus  $n_e \propto \rho_0 \propto R^{3/2}$ . In this limit,  $y_{\text{eff}} \propto R^{-3}$ , i.e., it decreases sharply with increasing radial distance. The opposite limit is to assume the electron density roughly constant or only slightly increasing with  $R$  (see, e.g. Figure 4 of Paper III), which follows from an interplay between the higher midplane density and a sharper decrease of vertical density profile for increasing radial coordinate. Even in this extreme case,  $y_{\text{eff}}$  decreases faster than linearly with increasing  $R$ . These considerations explain why the Comptonization influences mostly the inner annuli, while the outer annuli are influenced progressively less and less.

To see the effects of Comptonization on the hydrogen and He II Lyman edges more clearly, we present in Figure 7 a blow-up of Figure 5. It is clear Comptonization indeed considerably smears the He II Lyman edge. The hydrogen Lyman edge is smeared as well, although the effect is much smaller because Comptonization is much less efficient at the relatively low frequencies corresponding to the hydrogen Lyman edge.

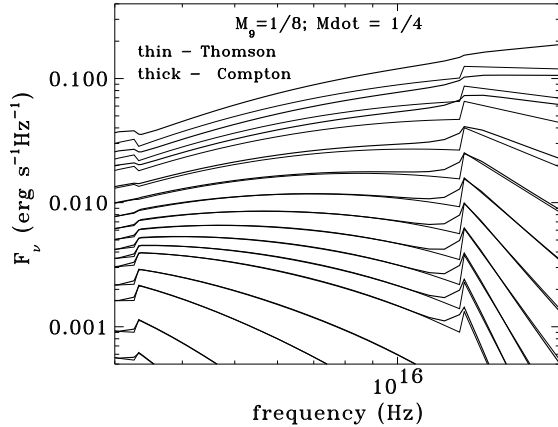


FIG. 7— A blow-up of Figure 5 showing the region of the hydrogen and He II Lyman edges. From top to bottom, the curves correspond to local emergent flux for the individual annuli at radii  $R/R_g = 2, 3, 4, 5, 6, 7, 8, 9, 10, 12, 14, 16, 18, 20, 25$ , and  $30$ . Thin lines represent the models from Paper III computed without Comptonization, and thick lines represent the models with Comptonization.

Finally, Figure 8 presents disk-integrated spectra for the above disk model. As in Paper III, the spectrum is found by integrating the total emergent intensity over the disk surface using our relativistic transfer function code (Agol 1997). The transfer function computes the trajectories of photons from infinity to the disk plane, finding the radius, redshift, and intensity at each angle at infinity for a given observation angle (Cunningham 1975). We neglect the effects of radiation that returns to the accretion disk.

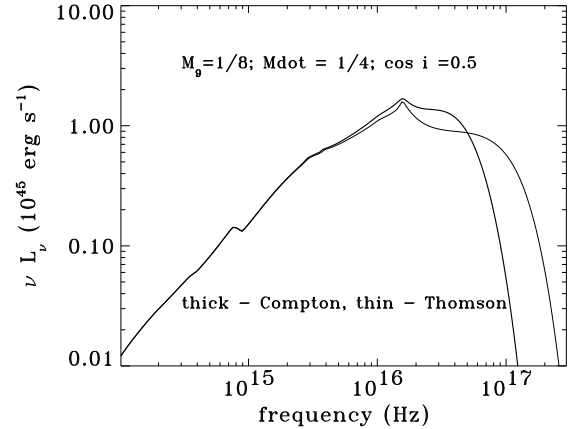


FIG. 8— Integrated spectral energy distribution  $\nu L_\nu$  (in  $\text{erg s}^{-1}$ ) for a disk with  $M = (1/8) \times 10^9 M_\odot$ ,  $\dot{M} = 1/4 M_\odot \text{ yr}^{-1}$ , (i.e.  $L/L_{\text{Edd}} = 0.3$ ), and  $\cos i = 0.5$ , for the model with (bold line) and without (thin line) Comptonization.

Comptonization hardly affects the optical and ultraviolet portions of the integrated spectrum, but it has a more dramatic effect at higher energies. The flux distribution around the He II Lyman limit is generally smoother; the flux in the region between  $2 \times 10^{16}$  and  $5 \times 10^{16}$  Hz (i.e., roughly between 0.1 and 0.2 keV) is about 30% larger if Comptonization is taken into account. About 10 percent of the total luminosity is shifted from the high energy tail (above  $6 \times 10^{16}$  Hz) to the peak of the spectrum (between  $1.5$  and  $4 \times 10^{16}$  Hz.)

We stress that, because they had larger central masses and therefore lower central temperatures, the effects of Comptonization for all other disks presented in Paper III should be smaller. Therefore, we conclude that neglecting Comptonization made little difference to the grid of models presented in that paper. This conclusion is in general agreement with the results of Laor & Netzer (1989), who found Comptonization to be unimportant for disks with  $T_{\text{eff}} \approx 10^5$  K.

#### 4.2. Comparison with Previous studies

Studies of the influence of Comptonization on disk atmospheres were pioneered by Ross, Fabian, & Mineshige (1992 - hereafter referred to as RFM). We now present a comparison with the models of RFM, who computed models of AGN accretion disks taking into account the effects of Compton scattering and some NLTE effects. Specifically, they assumed a constant (depth-independent) density in the  $z$ -direction, and solved the energy balance equation, the radiative transfer equation (but in the diffusion approximation), and the rate equations for the first three levels of H I and He II. In the latter equations, the radiative rates in the bound-bound transitions were treated by means of escape probability theory.

In order to compare our treatment of Comptonization to theirs, we have computed a set of test models as similar to RFM as possible. We have kept density fixed, and consider only three levels for H I and He II. Otherwise we have used our procedure to solve all the structural equations except hydrostatic equilibrium. Since our program does not use escape probabilities, we have determined the bound-bound radiative rates exactly, by solving the transfer equation with 15 frequency points per line.

We compare a single annulus at  $R/R_g = 9.8$ , taken from a disk with  $M = 10^7 M_\odot$  (Schwarzschild black hole) and

$L/L_{\text{edd}} = 0.3$  (i.e.  $\dot{M} = 0.1 M_{\odot}/\text{yr}$ ) to the corresponding RFM model, kindly supplied to us by Randy Ross – see Figure 9. Results for other annuli are analogous. The agreement of the computed flux in the continuum is very good, although there are some differences, particularly at the shortest and the longest wavelengths. The difference in the region of the flux peak is about 10%, which is likely explained by the RFM treatment of the inner boundary condition for the radiative transfer equation. For the frequencies at which the total effective optical thickness at the disk midplane is larger than unity, RFM assume that the radiation at the effective optical depth equal to unity is in LTE at the temperature given by an approximate expression [their Eqs. (15) and (16)]. In the present case, the effective optical thickness is slightly above unity for  $\nu < 10^{17}$ , and reaches values of about 10 at the He II Lyman discontinuity. Therefore the RFM treatment of the inner boundary condition is somewhat inaccurate for these frequencies.

The predicted profiles for the hydrogen and helium lines differ significantly, and some are even flipped from emission to absorption. This is very likely explained by differences in treating the lines, in particular the escape probability treatment adopted by RFM. Another reason may be a rather coarse wavelength resolution, and consequently low number of frequency points, adopted by RFM. As mentioned earlier, we will perform a detailed study of the effects of spectral lines on the vertical structure and emergent spectra for AGN disks in a future paper of this series.

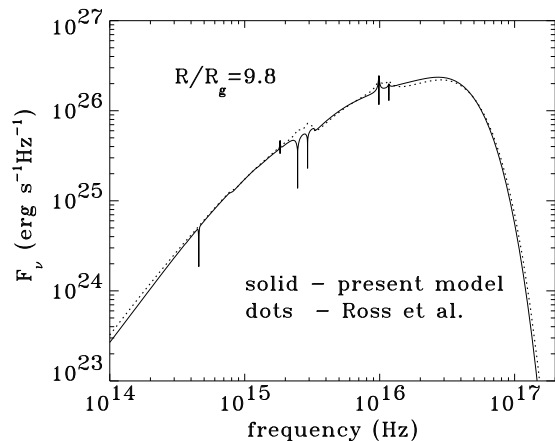


FIG. 9— A comparison of a sample model for one annulus at  $R/R_g = 9.8$ , for a disk with  $M = 10^7 M_{\odot}$  and  $L/L_{\text{edd}} = 0.3$  (i.e.  $\dot{M} = 0.1 M_{\odot}/\text{yr}$ ) computed by TLUSDISK (solid line) with the corresponding Ross, Fabian, Mineshige (1992) model (dotted line). The abscissa is the total flux from the annulus, i.e. the flux per unit area times the total area of the annulus, which is chosen to extend from  $R/R_g = 9.2$  to 10.4.

In a subsequent study, Shimura & Takahara (1993) developed a more accurate treatment of Comptonization. They considered, as in the present paper, the Kompaneets form of the Compton scattering emissivity, and solved the same list of structural equations as in this paper (hydrostatic equilibrium, energy balance, and the radiative transfer equation). However, they considered only free-free opacity, ignoring the many atomic opacity mechanisms, and they assumed a two-stream approximation for the radiative transfer (Rybicki & Lightman 1979). Unlike the present paper, they assumed separate energy

balance equations for the protons and the electrons. However, they also showed that there was very little difference between the two temperatures, supporting our approach of having the same kinetic temperature for all particles.

#### 4.3. Effects of Comptonization in hot disks

We have constructed several disk models. We consider three representative black-hole masses,  $M = 10^6, 10^7$ , and  $10^8 M_{\odot}$ . For all three masses we take  $L/L_{\text{edd}} \approx 0.3$ , i.e. mass accretion rates equal to 0.002, 0.02, and  $0.2 M_{\odot} \text{ yr}^{-1}$ , respectively. We assume a maximum rotation Kerr black hole. For each disk, we consider two values of the viscosity parameter  $\alpha$ : 0.1 and 0.01. Analogously to Paper III, we take the individual annuli for the radial coordinates  $R/R_g$  (with  $R_g = GM/c^2$  being the gravitational radius) equal to 1.5, 2, 2.5, 3, 3.5, 4, 5, 6, 7, 8, 9, 20, 12, 15, 20, 25, 30, 40, 50, 60, 70, 80, 90, 100, 150, 200, 250, 300, 400, 500, 600, 700, 800, 900, 1000, 1200, and 1500. A vertical structure model is computed for all annuli for which the effective temperature is higher than 5000 K; the cooler annuli are assumed to radiate as black bodies.<sup>2</sup> The outer edge of the disk is chosen to be the radius at which  $T_{\text{eff}}$  reaches 1000 K.

We first show the temperature structure for four representative annuli of the disk with  $M = 10^6 M_{\odot}$ ,  $\dot{M} = 0.002 M_{\odot} \text{ yr}^{-1}$ , and  $\alpha = 0.1$  and 0.01 – see Figure 10.

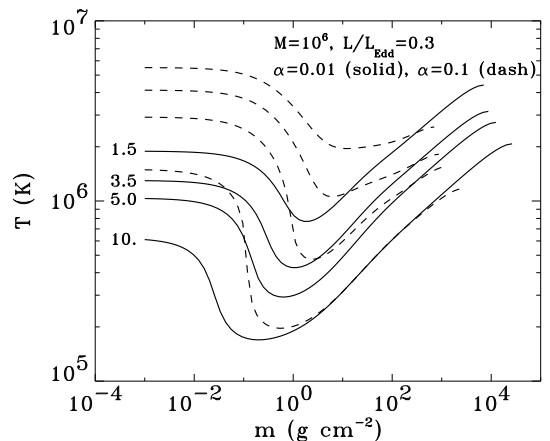


FIG. 10— Temperature as a function of depth for several representative annuli of the disk for  $M = 10^6 M_{\odot}$ ,  $L/L_{\text{edd}} \approx 0.3$ ; with  $\alpha = 0.01$  (solid lines), and  $\alpha = 0.1$  (dashed lines). From top to bottom, the curves correspond to radii  $R/R_g = 1.5, 3.5, 5$ , and 10.

The figure illustrates several interesting features. First, it shows the dependence of the surface temperature on both effective temperature and total optical thickness, and thus on the value of  $\alpha$ . We recall that the total thickness of the disk is inversely proportional to  $\alpha$  (Paper III). The hottest annulus has an effective temperature  $\approx 8 \times 10^5$  K. The total optical thickness at the disk midplane is approximately 240 for the  $\alpha = 0.1$  disk, and 2400 for the  $\alpha = 0.01$  disk. The mean photon destruction parameter for the  $\alpha = 0.1$  disk is about  $10^{-6}$ , while that for the  $\alpha = 0.01$  disk is about  $10^{-5}$ . From Figure 2 we deduce that  $T_0/T_{\text{eff}}$  should be around 6 and 2, respectively, for these two disks, which is indeed verified by numerical calculations.

<sup>2</sup>We used the same prescription in Paper III. Note that there were typos in that paper: the transition temperature was stated to be 4000 K, whereas in fact it was chosen to be 5000 K.

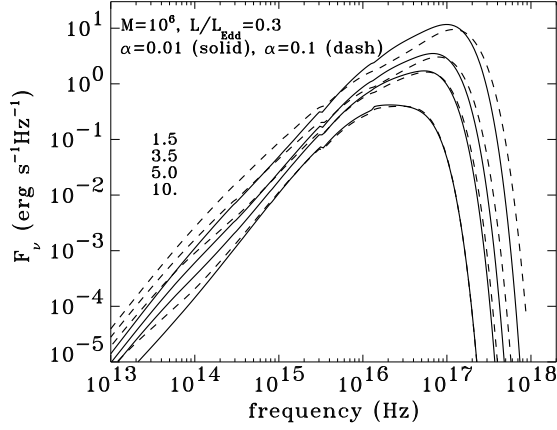


FIG. 11– Local emergent flux for several representative annuli of the disk for  $M = 10^6 M_\odot$ ,  $L/L_{\text{Edd}} \approx 0.3$ ; with  $\alpha = 0.01$  (solid lines), and  $\alpha = 0.1$  (dashed lines). The curves correspond to radii  $R/R_g$  (from top to bottom) 1.5, 3.5, 5, and 10.

Finally, the corresponding emergent flux for the four annuli displayed in Figure 10 are shown in Figure 11. Higher values of  $\alpha$  have somewhat suppressed flux near the peak and enhanced flux at low and high frequencies. This effect is most pronounced at small radii, i.e. lower total optical thickness. To understand the behavior of the emergent flux, we display the effective Compton  $y$ -parameter and other interesting quantities for the annulus at  $R/R_g = 1.5$  of the disk with  $M = 10^6 M_\odot$ ,  $L/L_{\text{Edd}} \approx 0.3$ , and for the two values of  $\alpha$  – see Figure 12. This plot is analogous to Figure 6.

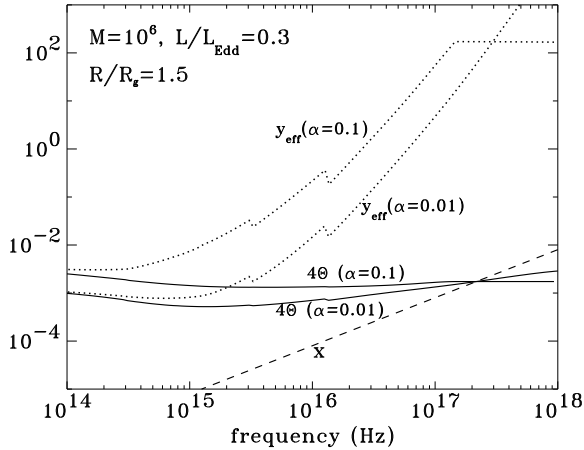


FIG. 12– Computed values of  $4\Theta(T_\nu^*)$ ,  $x$ , and the Compton parameter  $y_{\text{eff}}$  for the annulus at  $R/R_g = 1.5$  of the disk with  $M = 10^6 M_\odot$ ,  $L/L_{\text{Edd}} \approx 0.3$ , and for  $\alpha = 0.01$  and 0.1.

Increasing  $\alpha$  decreases density in the disk, leading to greater Comptonization because  $y_{\text{eff}} \propto n_e^{-18/15}$  – see equation (64). In line with this expectation,  $y_{\text{eff}}$  in the models with  $\alpha = 0.1$  is more than an order of magnitude greater than in the models with  $\alpha = 0.01$ . This is indeed nicely seen in Figure 12. The frequency where  $4\Theta(T_\nu^*) \approx x$  is about  $2 \times 10^{17}$  Hz. However, the disk with  $\alpha = 0.1$  becomes effectively thin at  $\nu \approx 1.3 \times 10^{17}$  Hz, while the annulus with  $\alpha = 0.01$  is effectively thick for all frequencies, so that  $y_{\text{eff}}$  keeps increasing with frequency. In the model with  $\alpha = 0.1$ , Comptonization is more efficient at removing photons from the frequency range  $\nu < 2 \times 10^{17}$  Hz to

the region around  $2 \times 10^{17}$  Hz, so that the flux for lower frequencies is depressed compared to the model with  $\alpha = 0.01$ . For higher frequencies, Comptonization is in contrast more efficient for the model with  $\alpha = 0.01$ , which leads to a larger shift of photon energies towards lower frequencies, thus resulting in a lower flux for the model with  $\alpha = 0.01$ .

#### 4.4. Effects of metals

We first computed a series of test models in order to determine which metals must be treated in detail. These models had the full array of metals as discussed in Sect 2, i.e., H, He, C, N, O, Ne, Mg, Si, S, Ar, Ca, Fe, and Ni. These test models showed that Mg, Si, S, Ca, and Ni have only a marginal influence on models (both on the structure and emergent spectral energy distribution), so we have computed most models with only H, He, C, N, O, Ne, and Fe.

Figure 13 shows a comparison between models computed assuming a simple H-He chemical composition and models with metals. We plot here the total integrated spectrum of the three representative disks. We also show the integrated spectrum assuming a black-body flux for each annulus. As in our previous models, the self-consistent treatment of radiation leads to a redistribution of flux from the optical and UV region to the EUV and soft X-ray region as compared to the integrated black-body energy distribution.

The effect of metals is relatively small; the only difference in the predicted spectra is seen in the high energy tails. Generally, the spectra begin to differ at a frequency about three times higher than the frequency where the emergent flux attains its maximum. The reason for this may be seen more clearly in Figure 14, where we present a comparison of the effective Compton  $y$ -parameter for a representative H-He model and for a model with metals, for a representative hot annulus of the disk with  $M = 10^6 M_\odot$ ,  $L/L_{\text{Edd}} \approx 0.3$ , and  $\alpha = 0.01$ . We do not show a comparison of local temperature for the models with metals to those of the H-He composition because the differences are very small. The metals thus do not influence the emergent radiation through their effects upon the vertical structure, but only through their effect on the thermal coupling parameter  $\epsilon$  and consequently on the efficiency of Comptonization.

We see in Figure 14 that in contrast to the H-He model, the effective Compton  $y$ -parameter reaches a maximum in the region  $10^{17} \lesssim \nu \lesssim 2 \times 10^{17}$  because of the effects of metals, in particular the O VIII Lyman edge at  $\nu \approx 2 \times 10^{17}$  Hz. For higher frequencies, Comptonization is thus not very efficient. The emergent flux is thus roughly given by the modified black-body spectrum corresponding to the local temperature at the effective depth of formation. As we see in Figure 14, this temperature, which is proportional to  $\Theta$ , is decreased by the influence of metals for  $\nu \lesssim 2 \times 10^{17}$ , and so is the emergent flux.

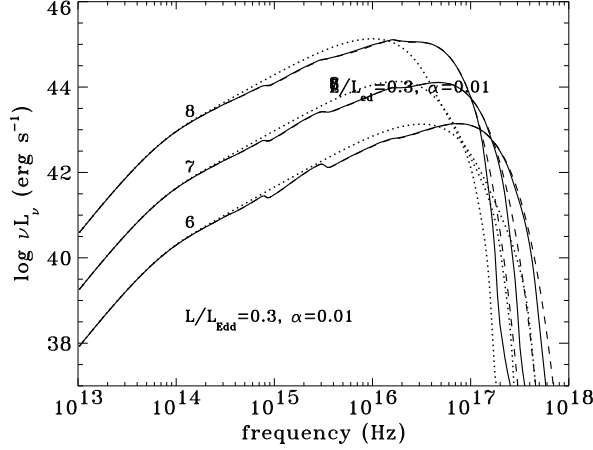


FIG. 13– Integrated spectral energy distribution  $\nu L_\nu$  for three representative disks for  $M = 10^6$ ,  $10^7$ , and  $10^8 M_\odot$ ,  $L/L_{\text{Edd}} \approx 0.3$ ,  $\alpha = 0.01$ . The solid lines show models with metals, while the dashed lines show H-He models. Dotted lines are the integrated energy distributions assuming the black-body flux for each annulus. The curves are labeled by the values of  $\log M$ .

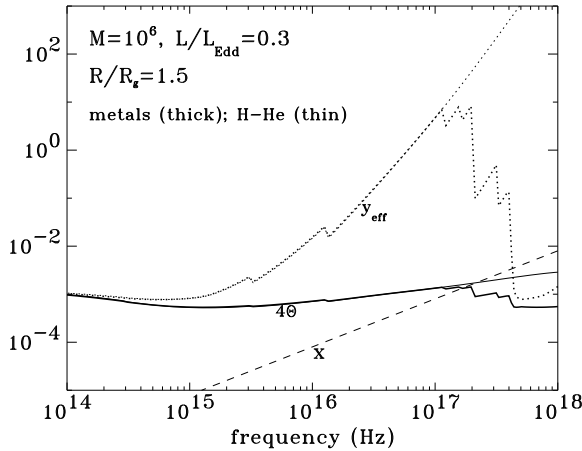


FIG. 14– Computed values of  $4\Theta(T_\nu^*)$ ,  $x$ , and the Compton parameter  $y_{\text{eff}}$  for the annulus at  $R/R_g = 1.5$  of the disk with  $M = 10^6 M_\odot$ ,  $L/L_{\text{Edd}} \approx 0.3$ , and  $\alpha = 0.01$ . Thick lines represent the values for the model with metals, while the thin lines represent the values for the H-He model. The influence of metal edges upon the thermal destruction parameter  $\epsilon$  and thus  $y_{\text{eff}}$  are clearly seen. As is illustrated in Figure 16, the discontinuities in the curve of  $4\Theta(T_\nu^*)$  correspond (with increasing frequency) to the Lyman edges of H I, He II, C VI, N VII, O VIII, Ne X, and Fe XXIV.

In order to show the effects of metals more clearly, we plot in Figure 15 the ratio of the integrated flux for models with metals to those for the H-He composition, for the same disks as shown in Figure 13. The reason for a different shape of the curves for different black hole masses is easy to understand. In the present circumstances, the metals contribute significantly to the opacity only through K-shell ionization of C, N, O, and Ne, and L-shell ionization of Fe. Only those species with edges well above  $kT$  retain significant abundance. Consequently, as the characteristic temperature rises, the mix of heavy elements contributing to the high-frequency opacity shifts to higher atomic number and therefore opacity at higher frequencies. All edges appear blue-shifted in the integrated spectrum due to relativistic effects.

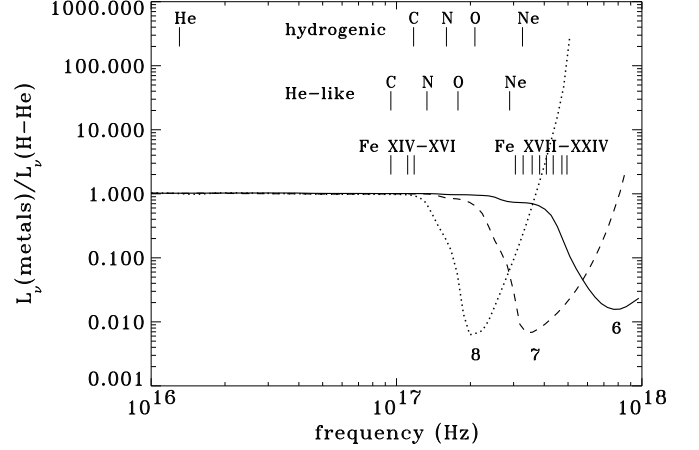


FIG. 15– The ratio of integrated spectral energy distribution  $L_\nu$  for the model with metals to that for the H-He model for three representative disks with  $M = 10^6$ ,  $10^7$ , and  $10^8 M_\odot$ ,  $L/L_{\text{Edd}} \approx 0.3$ , and  $\alpha = 0.01$ . The curves are labeled by the values of  $\log M$ . We also show the positions of the photoionization edges of the hydrogenic and He-like ions of He, C, N, O, and Ne, and of various ions of iron.

The effects of changing the value of the viscosity parameter  $\alpha$  are displayed in Figure 16. Here we display the same models as in Figure 13, with metals, together with analogous models for  $\alpha = 0.1$ . As before, we plot the black-body energy distribution as well. The spectral energy distributions coincide for  $\nu < 10^{15}$  Hz; therefore only the high energy portions of the spectra are shown.

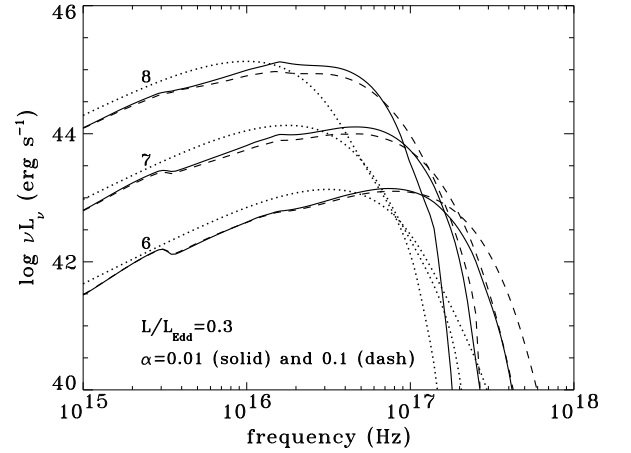


FIG. 16– Integrated spectral energy distributions  $\nu L_\nu$  for three representative disks with  $M = 10^6$ ,  $10^7$ , and  $10^8 M_\odot$ ,  $L/L_{\text{Edd}} \approx 0.3$ , computed with the influence of metal continuum opacities. Solid lines show models with  $\alpha = 0.01$ , while dashed lines show models with  $\alpha = 0.1$ . Dotted lines are the integrated energy distributions assuming the black-body flux for each annulus. The curves are labeled by the values of  $\log M$ .

Models with  $\alpha = 0.1$  generally exhibit a lower flux at frequencies below and around the maximum of flux, while the flux for high  $\alpha$  models is much larger for the high-frequency region. This behavior is easily understood from the discussion of the individual annuli presented in the Sect. 4.2. Interestingly, the flux for a model with  $\alpha = 0.1$  for a given  $M$  is very close to the flux predicted for a model with  $\alpha = 0.01$  and  $M$  about an order of magnitude lower! We also conclude that for the hot disks, at least those considered in the present paper, the effects of chang-

ing the value of the viscosity parameter  $\alpha$  are *more important* than the effects of metal continuum opacities.

Finally, as a reference point for later work that examines surface ionization response to different heat deposition laws, we show the ionization structure for three representative annuli of the disk with  $M = 10^6 M_\odot$ , namely the hottest annulus,  $R/R_g = 1.5$  with  $T_{\text{eff}} = 807,000$  K; an intermediate annulus,  $R/R_g = 15$  with  $T_{\text{eff}} = 207,000$  K; and a “cool” annulus,  $R/R_g = 150$  with  $T_{\text{eff}} = 40,000$  K. We show the ionization for two species: oxygen, which is a representative for the light metals; and for iron. The knowledge of ionization balance is important to show us what are the most important opacity sources in the X-ray region. The results are shown in Figure 17 for oxygen, and Figure 18 for iron. The curves are labeled by the effective charge of the ion, i.e., “1” denoting neutrals, “2” once ionized, etc. The label appears close to the position of the maximum number density of the given ion.

Oxygen is essentially fully stripped in the hottest annulus throughout the whole vertical extent; while He-like oxygen (O VII) dominates around  $\tau \approx 1$  for the intermediate annulus. In the cool annulus, O III and IV are dominant stages around a Rosseland mean optical depth  $\tau \approx 1$ , while O V and VI dominate deeper down. The ionization of iron is shown in Figure 18. The dominant stages of iron are Fe XXII - XXV for the hot annulus; Fe XV - XVII for the intermediate annulus, and Fe IV - VII for the cool annulus.

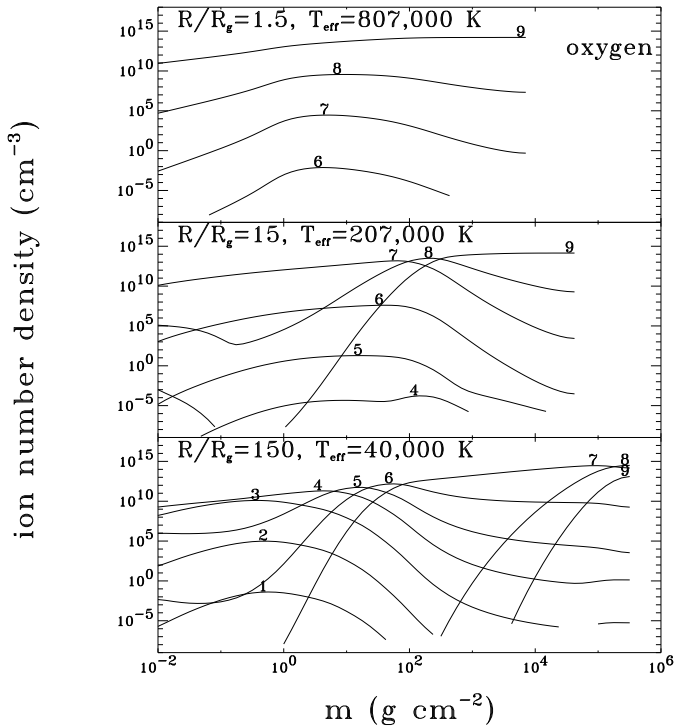


FIG. 17— Ionization structure of oxygen for three representative annuli of a disk model with  $M = 10^6 M_\odot$ ,  $L/L_{\text{Edd}} \approx 0.3$ , and  $\alpha = 0.01$ , at radial distances  $R/R_g = 1.5$ , 15, and 150. These annuli have effective temperatures approximately 807,000; 207,000; and 40,000 K, respectively. The abscissa is the column mass in  $\text{g cm}^{-2}$  and the ordinate is the ion number density in  $\text{cm}^{-3}$ . The curves are labeled by the effective charge of the ion, i.e., “1” denoting neutrals, “2” once ionized, etc.

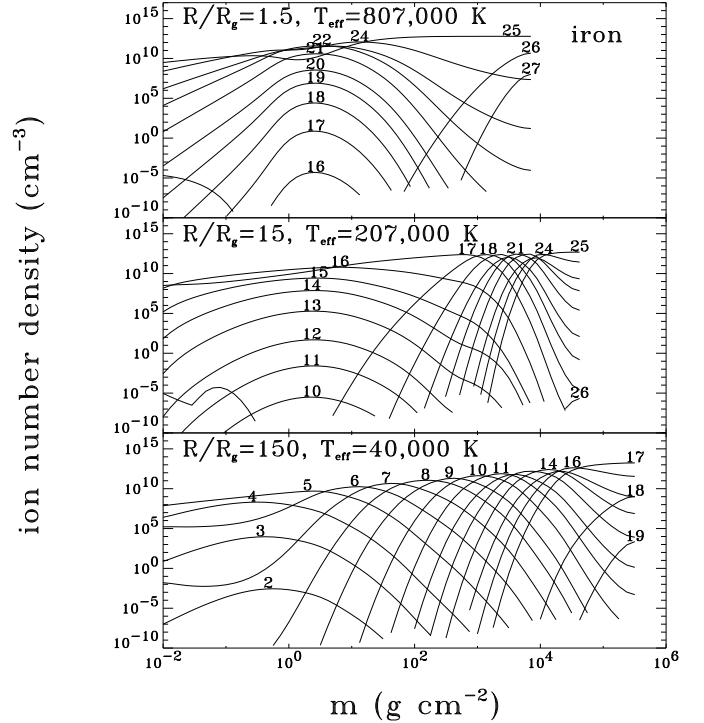


FIG. 18— The same as in Figure 17, but for iron.

## 5. DISCUSSION

### 5.1. Effect of Comptonization on H and He Edges

The observed absence of edge features at the hydrogen Lyman limit has been a commonly cited problem with accretion disk models of AGN. As we discussed extensively in Paper III, our disk models do not exhibit such features for accretion rates which are reasonable fractions of the Eddington limit, at least for the high black hole masses considered there. Comptonization only reinforces this conclusion, because it tends to smear out flux discontinuities (Czerny & Zbyszewska 1991). This is clear in the spectra of individual annuli shown in Figure 7. The effect is most dramatic for the HeII Lyman edge, which occurs at the high frequencies where Comptonization is most important, making it a much smoother feature (cf. Figure 8).

Our integrated disk spectra in Figure 13 show that the H and He II Lyman edges become more pronounced as the black hole mass is lowered. This effect is easily understood. The vertically averaged density as a function of  $R/R_g$  scales as (see Paper II)  $\bar{\rho} \propto (R/R_g)^{3/2} O(R/R_g) M \dot{M}^{-2} \alpha^{-1}$ , where the factor  $O(R/R_g)$  accounts for relativistic corrections. Since we consider models with fixed  $L/L_{\text{Edd}}$ , we have  $L/L_{\text{Edd}} \propto \dot{M}/M = \text{const}$ , i.e.,  $\dot{M} \propto M$ , so that the density scales for our set of models as  $\bar{\rho} \propto M^{-1} \alpha^{-1}$ . The models with lower mass have higher density, and therefore higher thermal coupling parameter  $\epsilon$ , so that the bound-free edges are stronger. The above considerations also indicate that the edges are weaker for higher values of  $\alpha$  (cf. Figure 16). Our results suggest that it might be easier to find broadened edge features in Seyferts rather than quasars, although one would have to look out to reasonable redshifts in order to avoid Galactic interstellar absorption.

### 5.2. Metal Opacities and Soft X-ray Emission

In these disks, whose heating rate per unit mass is either constant or declines toward the disk surface, the prime effect of

heavy element K-shell opacity is to partially suppress emission in the soft X-ray bands affected by these photoionization edges. The particular edges that most powerfully affect the spectrum depend on the central mass, rising in energy as the central mass decreases (Figure 15). To a very rough approximation, the central energy of the edge that produces the greatest X-ray absorption scales as  $M^{-1/4}$ , similarly to the temperature scale in the disk. As a result of this additional opacity, flux is redirected to frequency bands with smaller opacity in the EUV (Figure 13).

However, there is reason to think this effect may be strongly model-dependent. As shown in Figure 16, its magnitude can be substantially altered by changes in the local column density (as parameterized, for example, by the stress parameter  $\alpha$ ). Thinner disks present less soft X-ray opacity, and therefore show weaker breaks in that region than do thicker disks. Similarly, if the heating rate per unit mass were to increase, rather than decrease, in the surface layers, these same features might swing into emission.

Observations of quasar spectra in the  $\sim 100 - 1000$  eV band reveal a complicated (and possibly contradictory) story. Low redshift radio-quiet quasars appear to be consistent with single steep power-laws with an average spectral slope of  $d \ln L_\nu / d \ln \nu \simeq -1.7$  (Laor et al. 1997). On the other hand, in many cases the spectra of lower luminosity nearby radio quiet AGN, while following power laws above  $\simeq 2$  keV, rise sharply at lower energies (Turner & Pounds 1989), producing a so-called “soft excess”. Similarly, Blair et al. (2000) find that the composite X-ray spectra of quasars binned over various redshift intervals are best fit by a combination of a power-law and single-temperature blackbody. The power law component has a spectral slope of  $d \ln L_\nu / d \ln \nu \simeq -0.9$ , consistent with the 2–10 keV slope seen in nearby Seyferts. The blackbody component that they fit has a temperature that rises from  $\simeq 100$  eV at  $z \simeq 0$  to  $\simeq 270$  eV at  $z \simeq 2.5$ . The luminosity of this component is  $\simeq 10^{44}$  ergs  $s^{-1}$ , independent of redshift.

As shown in Figure 16, the spectral energy distributions expected from our disk models in the 0.2–2 keV ( $5 \times 10^{16} - 5 \times 10^{17}$  Hz) band show a broad range of slopes. At the highest energies they all show exponential rollovers, however, so the hard power-law spectra observed in AGN require a separate component. This is widely believed to be due to thermal Comptonization in a hot corona. A modification of our models to include increased viscous dissipation near the surface might be able to self-consistently produce such a corona, and we will explore this in a future paper.

Whether or not the models presented in this paper can provide good fits to the soft excess alone is unclear. Our models require  $L/L_{\text{Edd}} < 0.3$  in order to be consistent with our assumption that the disk is geometrically thin. A black hole mass of at least  $10^8 M_\odot$  is required to produce observed quasar luminosities, and Figure 16 shows that our accretion disk models for such black holes will produce spectra that peak below 200 eV. This might nevertheless be consistent with the 270 eV temperatures of the Blair et al. blackbody components at high redshift. Our models are not well-fit by single temperature blackbodies near the peak, so detailed spectral fits are required.

Huge soft X-ray excesses are a hallmark of narrow line Seyfert 1 galaxies (Boller, Brandt, & Fink 1996). In order to explain the soft X-rays, accretion disk models of these sources are inevitably forced to high accretion luminosities (Eddington or above), if they are based on the assumption of local blackbody emission (e.g. Mineshige et al. 2000). However, our models shown in Figure 16 indicate that these high accretion rates may

not in fact be necessary. Comptonization extends the emission well beyond that expected from a multi-temperature blackbody model of the same disk. This might contribute substantially to the observed soft X-ray excesses in narrow line Seyfert 1s, particularly at the relatively low black hole masses that might exist in these sources.

### 5.3. Radiative vs. Convective Heat Transport

We have assumed throughout the present paper that heat is transported vertically through the disk by radiative transfer. However, it turns out that all our disk models are convectively unstable. Away from ionization zones, the square of the Brunt-Väisälä frequency in the optically thick limit may be written as

$$N^2 = g \frac{d \ln \rho}{dz} \left( \frac{3P}{5P_{\text{gas}} + 4P_{\text{rad}}} \right) \left[ \frac{d \ln P}{d \ln \rho} - \left( \frac{d \ln P}{d \ln \rho} \right)_{\text{ad}} \right], \quad (65)$$

where the adiabatic gradient is

$$\left( \frac{d \ln P}{d \ln \rho} \right)_{\text{ad}} = \frac{5P_{\text{gas}} + 4P_{\text{rad}}}{3P}, \quad (66)$$

and  $P = P_{\text{rad}} + P_{\text{gas}}$  is the total (radiation plus gas) pressure. Note that the adiabatic gradient is  $4/3$  for a radiation pressure dominated medium, but  $5/3$  for a gas pressure dominated medium. Equation (65) shows that convective instability occurs when  $d \ln P / d \ln \rho$  exceeds the adiabatic gradient, with a characteristic growth rate of order the orbital frequency. Figure 19 depicts  $d \ln P / d \ln \rho$  as a function of column density for a number of annuli in our  $M = 10^6 M_\odot$ ,  $L = 0.3 L_{\text{Edd}}$ ,  $\alpha = 0.01$  model. We see that all our annuli are convectively unstable at high column densities. Photon diffusion is not included in equation (65), but the effect of a long photon mean free path near the photosphere would be to diminish the radiation pressure contribution to the adiabatic gradient, which therefore approaches  $5/3$ .

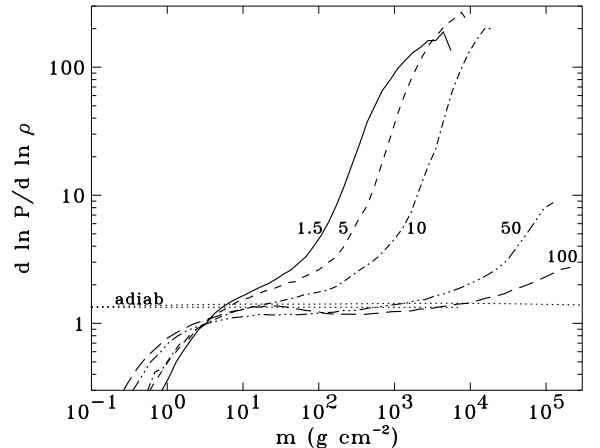


FIG. 19— Plot of the logarithmic gradient  $d \ln P / d \ln \rho$  as a function of column density for a number of annuli in the  $M = 10^6 M_\odot$ ,  $L = 0.3 L_{\text{Edd}}$ ,  $\alpha = 0.01$  model. The curves are labeled by the value of  $R/R_g$ . Dotted lines show the adiabatic gradient for the hottest annulus ( $R/R_g = 1.5$  – lower curve), and for the coolest annulus ( $R/R_g = 100$  – upper curve). In both cases, the adiabatic gradient is close to  $4/3$ , although it is higher for the cooler model, where the gas pressure makes a non-negligible contribution.

These instabilities depend of course on our assumed vertical dissipation profile. At the present time this profile is un-

known, although numerical simulations of the nonlinear development of the magneto-rotational instability are beginning to address this question, at least in gas pressure dominated disks (e.g. Miller & Stone 2000). It is nevertheless clear that our models are not self-consistent, and convective heat transport should be included. How this will affect the spectrum is unclear. While the scattering photospheres appear to be convectively stable, the continuum is formed in deeper, potentially unstable layers. More seriously, hydrodynamical simulations show that convective heat transport changes the overall heat content in the disk, altering the scale height and surface gravity of the photosphere (Agol et al. 2000). These simulations also produce an approximately isentropic configuration (at least when horizontally averaged), similar to what is seen in convection zones in stars. Assuming that magnetic fields do not change things (see, however, Hawley, Balbus, & Stone 2001), the assumption of constant entropy may provide a good first approximation to convective heat transport in unstable zones. We will address convective heat transport in disks in a future paper.

## 6. CONCLUSIONS

We have extended our modeling procedure described in the previous papers of this series in two respects. First, we have self-consistently included the effects of Compton scattering, both on the disk structure and on the emergent radiation. Second, we have included the effects of continuum opacities of the most important metals (C, N, O, Ne, Mg, Si, S, Ar, Ca, Fe, Ni).

The present models are thus based on the following assumptions:

- (i) The energy is generated by turbulent viscous dissipation, with the vertically-averaged viscosity described through the Shakura-Sunyaev parameter  $\alpha$ .
- (ii) The kinematic viscosity is constant with depth.
- (iii) Convection and conduction are neglected.
- (iv) No external irradiation or self-irradiation of the disk is considered.
- (v) Effects of line opacity are neglected.

The underlying assumption, not listed here, is that the 1-D approach is appropriate, i.e., that the disk may be described as a set of mutually non-interacting, concentric annuli.

We have also developed a simple analytic model that provides an estimate of the vertical temperature structure of the disk in the presence of Comptonization. An interesting by-product of this model is an estimate of the surface temperature. In particular, we have shown under which conditions a hot outer layer (a “corona”) is formed.

We have recomputed a number of models from the very large central-mass grid of Hubeny et al. 2000 (Paper III) with Comptonization taken into account, and showed that the predicted disk-integrated spectra differ only modestly from the previous

models. We have concluded that the grid of models from Paper III is not significantly plagued by neglecting Comptonization, except perhaps for the very hottest (smallest central mass) models of the sample. We have also compared our results to analogous models of Ross, Fabian, & Mineshige (1992). The agreement of the computed continuum flux is very good, although there are some differences, particularly at the shortest and the longest wavelengths. The predicted profiles for the hydrogen and helium lines differ significantly, which is very likely explained by differences in treating the lines, in particular by the escape probability treatment adopted by Ross et al.

We have also computed a set of vertical structure models for black hole masses of  $10^6$ ,  $10^7$ , and  $10^8 M_\odot$ , total luminosity  $L/L_{\text{Edd}} \approx 0.3$ , and for two values of the  $\alpha$  parameter: 0.1, and 0.01. Unlike the previous papers of this series, we consider a depth-independent kinematic viscosity. The main effect of Comptonization in this mass range is to transfer about 10 percent of the total luminosity from the high energy tail (above  $6 \times 10^{16}$  Hz) to the peak of the spectrum (between 1.5 and  $4 \times 10^{16}$  Hz.) We have computed a number of tests, and found that for the physical conditions studied in this paper (temperatures up to  $10^7$  K), the effects of Mg, Si, Ca, and Ni are negligible. We have shown that the effects of other metals are still relatively modest. The only significant differences in the predicted spectra occur in the high-frequency tails of the spectra, where the flux is already rather low. Interestingly, the effects of changing the viscosity parameter  $\alpha$  from 0.01 to 0.1 are found to be larger than the effects of metals. Models with  $\alpha = 0.1$  generally exhibit a lower flux at frequencies below and around the maximum of flux, while the flux for high  $\alpha$  models is much larger for the high-frequency region.

The effects studied in this paper are most dramatic in the EUV/soft X-rays. As shown in Figure 16, this high frequency region of the spectrum differs enormously from that expected from multitemperature blackbodies. Fits to the soft X-ray excesses of AGN which assume local blackbodies will necessarily require an artificially high accretion rate and accretion luminosity.

In future papers of this series, we will relax assumption (ii), and will compute models that allow for an increase of the heating rate (kinematic viscosity) with height, leading to the formation of very hot upper layers of the disk. We will also relax assumptions (iii), incorporating convective heat transport, and (v), studying the effects of line opacities on the disk structure in detail.

We thank Randy Ross for providing us with his model in digital form. We also thank Tim Kallman for sharing with us his collection of atomic data. This work was supported in part by NASA grant NAG5-7075.

## APPENDIX

### APPENDIX A: THE COMPTON SCATTERING SOURCE FUNCTION

We treat Comptonization in the non-relativistic, diffusion limit, where the exact integral over the redistribution function is approximated by a Kompaneets type operator. The general form of the radiative transfer equation for arbitrary geometries in this limit has been derived by Babuel-Peyrissac & Rouvillois (1969) and Nagirner & Poutanen (1993).<sup>3</sup> In the plane-parallel geometry considered here, the radiation field is axisymmetric, but still has a dependence on the polar direction cosine  $\mu$ . After integrating over azimuthal angles, we find that the contribution of Compton scattering to the right-hand side of the radiative transfer equation (i.e. sources minus

<sup>3</sup>The equations in these papers contain small typos which we have corrected.



sinks) is

$$\mu \left( \frac{\partial I}{\partial z} \right)^{\text{Compt}} = \frac{3}{16} n_e \sigma_T \int_{-1}^1 d\mu_1 [(I_1 - I)(A - 2B + C) + B(D + E)]. \quad (\text{A1})$$

For simplicity of notation here, we have dropped the frequency subscript,  $\nu$ . The specific intensity  $I \equiv I_\nu(\mu)$ , while  $I_1 \equiv I_\nu(\mu_1)$ .

Here,

$$A(\mu, \mu_1) = \alpha, \quad (\text{A2})$$

$$B(\mu, \mu_1) = x(\alpha - \beta), \quad (\text{A3})$$

$$C(\mu, \mu_1) = 2\Theta(8 - 8\gamma - 3\alpha + 2\beta), \quad (\text{A4})$$

$$D = \frac{h\nu^4}{kT} \left[ \frac{k^2 T^2}{h^2} \frac{\partial^2}{\partial \nu^2} \left( \frac{I_1}{\nu^3} \right) + \frac{kT}{h} \frac{\partial}{\partial \nu} \left( \frac{I_1}{\nu^3} \right) \left( 1 + \frac{c^2}{h\nu^3} I \right) \right], \quad (\text{A5})$$

and

$$E = 4 \left[ \frac{kT}{h} \nu^3 \frac{\partial}{\partial \nu} \left( \frac{I_1}{\nu^3} \right) + I_1 \left( 1 + \frac{c^2}{2h\nu^3} I \right) \right]; \quad (\text{A6})$$

where

$$x = \frac{h\nu}{m_e c^2}, \quad \Theta = \frac{kT}{m_e c^2}, \quad (\text{A7})$$

and where the matrices  $\alpha$ ,  $\beta$ , and  $\gamma$  are given by

$$\alpha(\mu, \mu_1) = 3\mu^2 \mu_1^2 - \mu^2 - \mu_1^2 + 3, \quad (\text{A8})$$

$$\beta(\mu, \mu_1) = 5\mu\mu_1 + 5\mu^3 \mu_1^3 - 3\mu^3 \mu_1 - 3\mu\mu_1^3, \quad (\text{A9})$$

$$\gamma(\mu, \mu_1) = \mu\mu_1, \quad (\text{A10})$$

so that  $\alpha$  is an even function of  $\mu$  or  $\mu_1$ , while  $\beta$  and  $\gamma$  are odd.

The radiative transfer equation is conveniently written by splitting the total absorption/emission term into four parts: absorption ( $\sigma_\nu I_\nu$ ), spontaneous emission ( $\eta_\nu$ ), stimulated emission ( $\eta_\nu^{\text{stim}} I_\nu$ ), and thermal absorption/emission ( $\kappa_\nu^{\text{th}}, \eta_\nu^{\text{th}}$ ), i.e.,

$$\mu \frac{\partial I_\nu}{\partial z} = -(\kappa_\nu^{\text{th}} + \sigma_\nu) I_\nu + \eta_\nu + \eta_\nu^{\text{th}} + \eta_\nu^{\text{stim}} I_\nu, \quad (\text{A11})$$

where

$$\sigma_\nu = \frac{3}{16} n_e \sigma_T \int_{-1}^1 d\mu_1 (A - 2B + C), \quad (\text{A12})$$

$$\eta_\nu = \frac{3}{16} n_e \sigma_T \int_{-1}^1 d\mu_1 [I_1 (A - 2B + C) + B(D' + E')], \quad (\text{A13})$$

$$\eta_\nu^{\text{stim}} = \frac{3}{16} n_e \sigma_T \frac{c^2}{2h\nu^3} \int_{-1}^1 d\mu_1 B \left[ \frac{2h\nu^4}{kT} \frac{kT}{h} \frac{\partial}{\partial \nu} \left( \frac{I_1}{\nu^3} \right) + 4I_1 \right], \quad (\text{A14})$$

where  $D'$  and  $E'$  are the  $D$  and  $E$  terms without the stimulated emission contributions, i.e.,

$$D' = \frac{h\nu^4}{kT} \left[ \frac{k^2 T^2}{h^2} \frac{\partial^2}{\partial \nu^2} \left( \frac{I_1}{\nu^3} \right) + \frac{kT}{h} \frac{\partial}{\partial \nu} \left( \frac{I_1}{\nu^3} \right) \right], \quad (\text{A15})$$

and

$$E' = 4 \left[ \frac{kT}{h} \nu^3 \frac{\partial}{\partial \nu} \left( \frac{I_1}{\nu^3} \right) + I_1 \right]. \quad (\text{A16})$$

We introduce the following notation

$$I'_\nu = \frac{\partial I_\nu}{\partial \ln \nu}, \quad I''_\nu = \frac{\partial^2 I_\nu}{\partial (\ln \nu)^2}. \quad (\text{A17})$$

so the  $D'$  and  $E'$  terms are written

$$D' = \frac{kT}{h\nu} (I''_1 - 7I'_1 + 12I_1) + (I'_1 - 3I_1), \quad (\text{A18})$$

$$E' = 4 \frac{kT}{h\nu} (I'_1 - 3I_1) + 4I_1, \quad (\text{A19})$$

and thus

$$x(D' + E') = \Theta I''_1 + (x - 3\Theta) I'_1 + xI_1. \quad (\text{A20})$$

After some algebra, we obtain for the individual terms

$$\sigma_\nu = n_e \sigma_T (1 - 2x), \quad (\text{A21})$$

$$\eta_\nu = \frac{3}{16} n_e \sigma_T \int_{-1}^1 d\mu_1 \{ [(1-x-6\Theta)\alpha + 16\Theta + (x+4\Theta)\beta - 16\Theta\gamma] I_1 \\ + (\alpha - \beta)(x - 3\Theta)I_1' + (\alpha - \beta)\Theta I_1'' \}, \quad (\text{A22})$$

and

$$\eta_\nu^{\text{stim}} = \frac{3}{16} n_e \sigma_T \frac{c^2}{2h\nu^3} \int_{-1}^1 d\mu_1 2x(\alpha - \beta)(I_1' - I_1). \quad (\text{A23})$$

The thermal terms  $\kappa_\nu^{\text{th}}$  and  $\eta_\nu^{\text{th}}$  contain bound-free, free-free, and possibly also bound-bound contributions from all transitions which are taken into account. The stimulated emission is treated as negative absorption, as is customary in astrophysical radiative transfer.

The Compton emission terms are more complicated than the thermal emission term  $\eta_\nu^{\text{th}}$  because they depend explicitly on angle. To write them in a more useful form, let us first introduce the traditional moments of the specific intensity, defined by

$$[J, H, K, N] \equiv \frac{1}{2} \int_{-1}^1 d\mu_1 I_1 \cdot [1, \mu_1, \mu_1^2, \mu_1^3]. \quad (\text{A24})$$

and also special “pseudo-moments” of the specific intensity with weights  $\alpha$ ,  $\beta$ , and  $\gamma$ , defined as

$$[\mathcal{J}_\alpha, \mathcal{J}_\beta, \mathcal{J}_\gamma] \equiv \frac{3}{16} \int_{-1}^1 d\mu_1 I_1 \cdot [\alpha, \beta, \gamma], \quad (\text{A25})$$

The pseudo-moments can be expressed through the ordinary moments as

$$\mathcal{J}_\alpha = \frac{3}{8} [(3 - \mu^2)J + (3\mu^2 - 1)K], \quad (\text{A26})$$

$$\mathcal{J}_\beta = \frac{3}{8} \mu [(5 - 3\mu^2)H + (5\mu^2 - 3)N], \quad (\text{A27})$$

$$\mathcal{J}_\gamma = \frac{3}{8} \mu H. \quad (\text{A28})$$

Because the pseudo-moments are integrals over matrices  $\alpha$ ,  $\beta$ , and  $\gamma$ , they are explicit functions of the angle,  $\mu$ . We may then also introduce moments of  $\mathcal{J}_\alpha$ ,  $\mathcal{J}_\beta$ , and  $\mathcal{J}_\gamma$ . The zero-order moments are given by

$$\frac{1}{2} \int_{-1}^1 \mathcal{J}_\alpha d\mu = J, \quad (\text{A29})$$

and (since  $\mathcal{J}_\beta$  and  $\mathcal{J}_\gamma$  are antisymmetric functions of  $\mu$ ),

$$\frac{1}{2} \int_{-1}^1 \mathcal{J}_\beta d\mu = \frac{1}{2} \int_{-1}^1 \mathcal{J}_\gamma d\mu = 0. \quad (\text{A30})$$

The first-order moments are given by

$$\frac{1}{2} \int_{-1}^1 \mathcal{J}_\alpha \mu d\mu = 0, \quad (\text{A31})$$

and

$$\frac{1}{2} \int_{-1}^1 \mathcal{J}_\beta \mu d\mu = \frac{2}{5} H, \quad \frac{1}{2} \int_{-1}^1 \mathcal{J}_\gamma \mu d\mu = \frac{1}{8} H. \quad (\text{A32})$$

Using the definitions of the optical depth,  $\tau_\nu$ , the photon destruction probability,  $\epsilon_\nu$ , and the scattering probability,  $\lambda_\nu$ , introduced in section 2.1, we obtain for the full, angle-dependent transfer equation

$$\mu \frac{\partial I_\nu(\mu)}{\partial \tau_\nu} = I_\nu(\mu) - \epsilon_\nu S_\nu^{\text{th}} - \lambda_\nu S_\nu^{\text{Compt}}(\mu), \quad (\text{A33})$$

where the (generally angle-dependent) “Compton source function” is given by

$$\begin{aligned} S_\nu^{\text{Compt}}(\mu) = & (1-x-6\Theta)\mathcal{J}_\alpha(\mu) + 6\Theta J + (x+4\Theta)\mathcal{J}_\beta(\mu) - 16\Theta\mathcal{J}_\gamma(\mu) + \\ & (x-3\Theta)[\mathcal{J}'_\alpha(\mu) - \mathcal{J}'_\beta(\mu)] + \Theta[\mathcal{J}''_\alpha(\mu) - \mathcal{J}''_\beta(\mu)] \\ & + I_\nu(\mu)b_\nu 2x[\mathcal{J}'_\alpha(\mu) - \mathcal{J}'_\beta(\mu) - \mathcal{J}_\alpha(\mu) + \mathcal{J}_\beta(\mu)], \end{aligned} \quad (\text{A34})$$

where the last term represents a contribution of the stimulated Compton scattering, with

$$b_\nu \equiv \frac{c^2}{2h\nu^3}. \quad (\text{A35})$$

So far we have not made any approximations beyond the Kompaneets limit of low photon energies ( $x \ll 1$ ) and low electron temperatures ( $\Theta \ll 1$ ). In particular, equation (A34) retains the full angle dependence of the Compton scattering source function. However, it is quite complicated to solve numerically, and we have made further approximations for all the calculations presented in this paper.

The first approximation deals with the stimulated emission term, which is nonlinear in the specific intensity. Fortunately, it is usually very small compared to the spontaneous term in our models, and could be neglected completely. We choose to retain it, and show how to treat the nonlinearity below. However, we approximate the angular dependence of the radiation field by replacing  $I_\nu(\mu)$  with  $J_\nu$  in the stimulated term.

More generally, we average the angle dependence of the Compton scattering source function by first taking moments of the transfer equation (A33). Using equations (A26) - (A32), the first and second moments are

$$\frac{\partial H_\nu}{\partial \tau_\nu} = J_\nu - \epsilon_\nu S_\nu^{\text{th}} - \lambda_\nu[(1-x)J_\nu + (x-3\Theta)J'_\nu + \Theta J''_\nu] - \lambda_\nu J_\nu b_\nu 2x(J'_\nu - J_\nu), \quad (\text{A36})$$

$$\frac{\partial K_\nu}{\partial \tau_\nu} = H_\nu - \lambda_\nu \frac{2}{5} [(x-\Theta)H_\nu - (x-3\Theta)H'_\nu - \Theta H''_\nu] - \lambda_\nu \frac{2}{5} J_\nu b_\nu 2x(H_\nu - H'_\nu). \quad (\text{A37})$$

We now assume that all terms on the right-hand side of equation (A37) are negligible with respect to the leading term  $H_\nu$ , so that the second moment equation is

$$\frac{\partial K_\nu}{\partial \tau_\nu} = H_\nu. \quad (\text{A38})$$

We now introduce the variable Eddington factor,

$$f_\nu \equiv K_\nu/J_\nu, \quad (\text{A39})$$

so that the two moment equations are combined to a single equation,

$$\frac{\partial^2(f_\nu J_\nu)}{\partial \tau_\nu^2} = J_\nu - \epsilon_\nu S_\nu^{\text{th}} - \lambda_\nu[(1-x)J_\nu + (x-3\Theta)J'_\nu + \Theta J''_\nu] - \lambda_\nu J_\nu b_\nu 2x(J'_\nu - J_\nu). \quad (\text{A40})$$

This equation is analogous to equations (1) and (8), and is used for computing the disk structure.

We introduce a set of discretized frequency points,  $\nu_i, i = 1, \dots, N$ ; with  $\nu_i < \nu_{i+1}$ . We denote  $I_i = I(\nu_i)$ . The frequency derivatives are treated using the following discrete representation. Let us first take internal frequency points,  $i = 2, \dots, N-1$ . Then

$$I'_i = c_i^- I_{i-1} + c_i^0 I_i + c_i^+ I_{i+1}, \quad (\text{A41})$$

$$I''_i = d_i^- I_{i-1} + d_i^0 I_i + d_i^+ I_{i+1}, \quad (\text{A42})$$

where the coefficients  $c_i^-$ ,  $c_i^0$ ,  $c_i^+$  are determined by the method of Chang & Cooper (1970), and

$$d_i^- = \frac{2}{\Delta_{i-1/2}\Delta_i}, \quad (\text{A43})$$

$$d_i^+ = \frac{2}{\Delta_{i+1/2}\Delta_i}, \quad (\text{A44})$$

$$d_i^0 = -d_i^- - d_i^+, \quad (\text{A45})$$

where

$$\Delta_{i-1/2} = \ln(\nu_i/\nu_{i-1}), \quad \Delta_{i+1/2} = \ln(\nu_{i+1}/\nu_i), \quad (\text{A46})$$

and

$$\Delta_i = \Delta_{i-1/2} + \Delta_{i+1/2}. \quad (\text{A47})$$

The boundary conditions in frequency space are written in the form of equations (A41) and (A42), with  $c_1^- = d_1^- = c_1^+ = d_1^+ = 0$ , and  $c_N^- = d_N^- = c_N^+ = d_N^+ = 0$ . At the lowest frequency we have, assuming the Rayleigh-Jeans form of the specific intensity, equation (13),

$$c_1^0 = 2, \quad d_1^0 = 4. \quad (\text{A48})$$

At the highest frequency we have either

$$c_N^0 = 3 - z, \quad d_N^0 = (3 - z)^2 - z, \quad (\text{A49})$$

(with  $z = h\nu/kT$ ) if we assume the Wien form of the specific intensity, equation (14); or

$$c_N^0 = -\beta, \quad d_N^0 = \beta^2, \quad (\text{A50})$$

if we assume the power-law form, equation (17).

We write the radiative transfer equation for the  $i$ -th frequency point as

$$\frac{\partial^2(f_i J_i)}{\partial \tau_i^2} = J_i - \epsilon_i S_i^{\text{th}} - \lambda_i [ (A_i J_{i-1} + B_i J_i + C_i J_{i+1}) - J_i (E_i J_i + U_i J_{i-1} + V_i J_{i+1}) ], \quad (\text{A51})$$

where

$$B_i = (1 - x_i) + (x_i - 3\Theta)c_i^0 + \Theta d_i^0, \quad (\text{A52})$$

$$A_i = (x_i - 3\Theta)c_i^- + \Theta d_i^-, \quad (\text{A53})$$

$$C_i = (x_i - 3\Theta)c_i^+ + \Theta d_i^+, \quad (\text{A54})$$

$$E_i = b_i 2x_i (c_i^0 - 1), \quad (\text{A55})$$

$$U_i = b_i 2x_i c_i^-, \quad (\text{A56})$$

$$V_i = b_i 2x_i c_i^+. \quad (\text{A57})$$

We now avoid the nonlinearity of the stimulated emission term by evaluating it partly by using “old” mean intensities. In other words, we replace  $B_i$  by  $B'_i$ , where

$$B'_i = B_i + E_i J_i^{\text{old}} + U_i J_{i-1}^{\text{old}} + V_i J_{i+1}^{\text{old}}. \quad (\text{A58})$$

The discretized transfer equation is then written

$$\frac{\partial^2(f_i J_i)}{\partial \tau_i^2} = J_i - \epsilon_i S_i^{\text{th}} - \lambda_i (A_i J_{i-1} + B'_i J_i + C_i J_{i+1}), \quad (\text{A59})$$

The final step is to consider a discrete representation of the differential term as in the standard Feautrier method (Mihalas 1978), viz.

$$\frac{\partial^2(f_i J_i)}{\partial \tau_i^2} \rightarrow \alpha_{i,d} J_{i,d-1} - \beta_{i,d} J_{i,d} + \gamma_{i,d} J_{i,d+1}, \quad (\text{A60})$$

where index  $d$  labels depth points, while  $i$  labels the frequency points. The coefficients  $\alpha$ ,  $\beta$ , and  $\gamma$  (not to be confused with the previously introduced angle-dependent matrices of Compton scattering) are given by

$$\alpha_{i,d} = f_{i,d-1} / (\Delta \tau_{i,d-1/2} \Delta \tau_{i,d}), \quad (\text{A61})$$

$$\gamma_{i,d} = f_{i,d+1} / (\Delta \tau_{i,d+1/2} \Delta \tau_{i,d}), \quad (\text{A62})$$

$$\beta_{i,d} = \frac{f_{i,d}}{\Delta \tau_{i,d}} \left( \frac{1}{\Delta \tau_{i,d-1/2}} + \frac{1}{\Delta \tau_{i,d+1/2}} \right), \quad (\text{A63})$$

and

$$\Delta \tau_{i,d-1/2} = \tau_{i,d} - \tau_{i,d-1}, \quad (\text{A64})$$

$$\Delta \tau_{i,d+1/2} = \tau_{i,d+1} - \tau_{i,d}, \quad (\text{A65})$$

$$\Delta \tau_{i,d} = (\tau_{i,d+1/2} + \tau_{i,d-1/2}) / 2. \quad (\text{A66})$$

The (second-order) boundary conditions are given by

$$\beta_{i,1} = 2f_{i,1}^H / \Delta \tau_{i,3/2} + 2f_{i,1} / (\Delta \tau_{i,3/2})^2, \quad (\text{A67})$$

$$\gamma_{i,1} = 2f_{i,2} / (\Delta \tau_{i,3/2})^2, \quad (\text{A68})$$

and

$$\beta_{i,D} = 2f_{i,D}/(\Delta\tau_{i,D-1/2})^2, \quad (\text{A69})$$

$$\alpha_{i,D} = 2f_{i,D-1}/(\Delta\tau_{i,D-1/2})^2. \quad (\text{A70})$$

The final discretized form of the transfer equation thus reads

$$-\alpha_{i,d}J_{i,d-1} - \gamma_{i,d}J_{i,d+1} + (\beta_{i,d} + 1 - \lambda_{i,d}B'_{i,d})J_{i,d} - \lambda_{i,d}A_{i,d}J_{i-1,d} - \lambda_{i,d}C_{i,d}J_{i+1,d} = \epsilon_{i,d}S_{i,d}^{\text{th}}. \quad (\text{A71})$$

The formal solution, i.e., a solution of the transfer equation with the known thermal source function,  $S_{i,d}^{\text{th}}$ , is obtained as follows. We organize the mean intensities in a set of column vectors

$$\mathbf{J}_i \equiv (J_{i,1}, J_{i,2}, \dots, J_{i,D})^T, \quad (\text{A72})$$

so that the mean intensity vector contains intensities in all depth points for a given frequency point  $i$ . The resulting discretized transfer equation reads

$$-\mathbf{A}_i\mathbf{J}_{i-1} + \mathbf{B}_i\mathbf{J}_i - \mathbf{C}_i\mathbf{J}_{i+1} = \mathbf{L}_i, \quad (\text{A73})$$

where the matrices  $\mathbf{B}$  are tridiagonal (because of the difference representations of the second derivative with respect to depth), while the matrices  $\mathbf{A}$  and  $\mathbf{C}$  are diagonal (because the terms containing the frequency derivatives are local in physical space).

The matrix elements are given by

$$(\mathbf{B}_i)_{d,d} = \beta_{i,d} + 1 - \lambda_{i,d}B'_{i,d}, \quad (\text{A74})$$

$$(\mathbf{B}_i)_{d,d-1} = -\alpha_{i,d}, \quad (\text{A75})$$

$$(\mathbf{B}_i)_{d,d+1} = -\gamma_{i,d}, \quad (\text{A76})$$

$$(\mathbf{A}_i)_{d,d} = \lambda_{i,d}A_{i,d}, \quad (\text{A77})$$

$$(\mathbf{C}_i)_{d,d} = \lambda_{i,d}C_{i,d}, \quad (\text{A78})$$

$$(\mathbf{L}_i)_d = \epsilon_{i,d}S_{i,d}^{\text{th}}. \quad (\text{A79})$$

Solution of equation (A73) is done by the standard Gauss-Jordan elimination, consisting of a forward elimination followed by a backsubstitution,

$$\mathbf{D}_i = (\mathbf{B}_i - \mathbf{A}_i\mathbf{D}_{i-1})^{-1} \mathbf{C}_i, \quad i = 2, \dots, D, \quad (\text{A80})$$

with

$$\mathbf{D}_1 = \mathbf{B}_1^{-1} \mathbf{C}_1, \quad (\text{A81})$$

and

$$\mathbf{Z}_i = (\mathbf{B}_i - \mathbf{A}_i\mathbf{D}_{i-1})^{-1} (\mathbf{L}_i + \mathbf{A}_i\mathbf{Z}_{i-1}), \quad i = 2, \dots, D, \quad (\text{A82})$$

with

$$\mathbf{Z}_1 = \mathbf{B}_1^{-1} \mathbf{L}_1. \quad (\text{A83})$$

The back substitution step is

$$\mathbf{J}_i = \mathbf{D}_i\mathbf{J}_{i+1} + \mathbf{Z}_i \quad i = 1, \dots, D-1, \quad (\text{A84})$$

with  $\mathbf{J}_N = \mathbf{Z}_N$ . Starting at  $i = 1$ , we compute successive values for  $\mathbf{D}_d$  and  $\mathbf{Z}_i$  through  $i = N-1$ . At the last point,  $i = N$ ,  $\mathbf{C}_N \equiv 0$  and hence  $\mathbf{D}_N = 0$ , and  $\mathbf{J}_N = \mathbf{Z}_N$ . Having found  $\mathbf{J}_N$ , we then perform successive back-substitutions into equation (A84) to find  $\mathbf{J}_i$ ,  $i = N-1, \dots, 1$ .

## APPENDIX B: TREATMENT OF DIELECTRONIC RECOMBINATION

In terms of a cross-section, the photoionization rate is given by (see, e.g., Mihalas 1978)

$$R_{ik} = \int_{\nu_0}^{\infty} \frac{4\pi}{h\nu} \sigma(\nu) J_{\nu} d\nu, \quad (\text{B1})$$

where  $\sigma(\nu)$  is the photoionization cross-section,  $\nu$  the frequency,  $\nu_0$  the frequency of the continuum edge, and  $J_{\nu}$  the mean intensity of radiation. The subscript  $i$  labels the starting level of the bound-free transition, while  $k$  labels the ending level (usually the ground state of the next higher ion).

The radiative recombination rate is given through detailed balance arguments (the Einstein-Milne relations for the continuum; see also Mihalas 1978) as

$$R_{ki} = n_e \phi_i(T) \int_{\nu_0}^{\infty} \frac{4\pi}{h\nu} \sigma(\nu) \left( \frac{2h\nu^3}{c^2} + J_{\nu} \right) \exp(-h\nu/kT) d\nu, \quad (\text{B2})$$

where  $n_e$  is the electron density, and  $\phi_i(T)$  the Saha-Boltzmann factor, given by (Mihalas 1978, p. 113)

$$\phi_i(T) = \left( \frac{h^2}{2\pi m k T} \right)^{3/2} \frac{g_i}{2g_k} \exp(h\nu_0/kT) \equiv C_I T^{-3/2} \frac{g_i}{g_k} \exp(h\nu_0/kT), \quad (\text{B3})$$

where  $g$  are the statistical weights. The first term on the right-hand side of equation (B2) represents spontaneous recombination, while the second term (proportional to  $J_\nu$ ) represents stimulated recombination.

We now use this to express the known dielectronic recombination rate through an artificial cross-section. For simplicity, we assume that

$$\sigma(\nu) = \sigma_0, \quad \text{for } \nu_0 \leq \nu \leq \nu_1, \quad (\text{B4})$$

and is zero everywhere else. We further assume that  $\nu_1/\nu_0 - 1 \ll 1$ , i.e., the frequency  $\nu_1$  is not very different from  $\nu_0$ . We further assume that the stimulated term is negligible (i.e.,  $J_\nu \ll 2h\nu^3/c^2$ ). The known recombination rate is given through the artificial cross-section as follows

$$R = n_e C_I T^{-3/2} \frac{g_i}{g_k} \exp(h\nu_0/kT) \int_{\nu_0}^{\nu_1} \frac{4\pi}{h\nu} \sigma_0 \frac{2h\nu^3}{c^2} \exp(-h\nu/kT) d\nu, \quad (\text{B5})$$

or

$$R = C_I \frac{8\pi}{c^2} n_e T^{-3/2} \frac{g_i}{g_k} \sigma_0 \int_{\nu_0}^{\nu_1} \nu^2 \exp[-h(\nu - \nu_0)/kT] d\nu. \quad (\text{B6})$$

The integrand is the product of two terms. The first one,  $\nu^2$ , varies slowly with  $\nu$  compared to the second, exponential, term. We may therefore remove the  $\nu^2$  term from the integral, replacing it with  $\bar{\nu}^2 \equiv [(\nu_0 + \nu_1)/2]^2 \simeq \nu_0^2$ , and performing the remaining integration analytically,

$$R = C_I \frac{8\pi k}{hc^2} n_e T^{-1/2} \frac{g_i}{g_k} \sigma_0 \bar{\nu}^2 [1 - \exp(-h\Delta\nu/kT)], \quad (\text{B7})$$

where  $\Delta\nu = \nu_1 - \nu_0$ . In the calculations reported in this paper, we used  $\nu_1 = 1.1\nu_0$ .

Consequently, the desired value of the cross-section,  $\sigma_0$ , is given by

$$\sigma_0 = R \frac{\sqrt{T}}{n_e} C_I \frac{hc^2}{8\pi k} \frac{g_k}{g_i} \frac{1}{\bar{\nu}^2} [1 - \exp(-h\Delta\nu/kT)]^{-1}. \quad (\text{B8})$$

Unlike the traditional cross-section,  $\sigma_0$  now generally depends on temperature and electron density. We treat this dependence exactly. Nevertheless, the dependence is rather weak because the dielectronic recombination rate is typically proportional to  $T^{-1/2}$ , so the  $T$ -dependence is contained essentially in the term  $\exp[-h(\nu_1 - \nu_0)/kT]$ , which is typically small compared to unity. Analogously, the dielectronic recombination rate is directly proportional to  $n_e$ , so the dependence of  $\sigma_0$  on physical parameters is to a large extent factored out, and one is left with  $\sigma_0$  essentially independent of state parameters.

## REFERENCES

- Abramowicz, M.A., Lanza, A., & Percival, M.J. 1997, *ApJ*, 479, 179  
 Abramowitz, M.A., & Stegun, I.A. 1972, *Handbook of Mathematical Functions*, (New York: Dover)  
 Agol, E. 1997, Ph.D. thesis, Univ. California, Santa Barbara  
 Agol, E., Krolik, J., Stone, J.M. & Turner, N.J. 2000, submitted to *ApJ*  
 Aldrovandi, S. M. V., & Péquignot, D. 1973, *A&A*, 25, 137  
 Arnaud, M., & Raymond, J. 1992, *ApJ*, 398, 394  
 Babuel-Peyrissac, J. P., & Rouvillois, G. 1969, *Journal de Physique*, 30, 301  
 Barfield, W. D., Koontz, G. D., & Huebner, W. F. 1972, *JQSRT*, 12, 1409  
 Blair, A.J., Stewart, G.C., Georgantopoulos, I., Boyle, B.J., Griffiths, R.E., Shanks, T., & Almaini, O. 2000, *MNRAS* 314, 138  
 Boller, Th., Brandt, W. N., & Fink, H. 1996, *A&A*, 305, 53  
 Chang, J.S., & Cooper, G. 1970, *J. Comp. Phys.* 6, 1  
 Cunningham, C. 1975, *ApJ*, 202, 788  
 Czerny, B., & Elvis, M. 1987, *ApJ*, 321, 305  
 Czerny, B., & Zbyszewska, M. 1991, *MNRAS*, 249, 634  
 Gammie, C. F. 1998, *MNRAS*, 297, 929  
 Hawley, J. F., Balbus, S. A., & Stone, J. M. 2001, *ApJ*, submitted [astro-ph/0103522]  
 Hubeny, I. 1988, *Comp. Phys. Commun.* 52, 103  
 Hubeny, I. 1990, *ApJ*, 351, 632  
 Hubeny, I., & Lanz, T. 1995, *ApJ*, 439, 875  
 Hubeny, I., & Hubeny, V. 1997, *ApJ*, 484, L37 (Paper I)  
 Hubeny, I., & Hubeny, V. 1998a, *ApJ*, 505, 558 (Paper II)  
 Hubeny, I., Agol, E., Blaes, O., & Krolik, J. H. 2000, *ApJ*, 533, 710 (Paper III)  
 Kaastra, J. S., & Mewe, R. 1993, *A&A Supp.*, 97, 443  
 Kallman, T. R. 2000, *XSTAR: A Spectral Analysis Tool*, Version 2.0 of the User's Guide, NASA Goddard Space Flight Center  
 Krolik, J. H. 1998, *ApJ*, 498, L13  
 Krolik, J. H. 1999, *Active Galactic Nuclei* (Princeton: Princeton Univ. Press)  
 Laor, A., Fiore, F., Elvis, M., Wilkes, B.J. & McDowell, J.C. 1997, *ApJ* 477, 93  
 Laor, A., & Netzer, H. 1989, *MNRAS*, 238, 897  
 Madej, J. 1989, *ApJ*, 339, 386  
 Madej, J. 1991, *ApJ*, 376, 161  
 Madej, J. 1998, *A&A* 340, 617  
 Madej, J., & Rozanska, A. 2001, *A&A* 363, 1055  
 Mihalas, D. 1978, *Stellar Atmospheres*, 2nd ed. (San Francisco: Freeman)  
 Miller, K. A., & Stone, J. M. 2000, *ApJ*, 534, 398  
 Mineshige, S., Kawaguchi, T., Takeuchi, M., & Hayashida, K. 2000, *PASJ*, 52, 499  
 Nagirner, D. I., & Poutanen, Yu. I. 1993, *Astron. Lett.*, 19, 262  
 Nandra, K., & Pounds, K. A. 1994, *MNRAS*, 268, 405  
 Nussbaumer, H., & Storey, P. J. 1983, *A&A*, 126, 75  
 Pomraning, G.C. 1973, *The Equations of Radiation Hydrodynamics* (Oxford: Pergamon)  
 Riffert, H., & Herold, H. 1995, *ApJ*, 450, 508  
 Ross, R. R., Fabian, A. C., & Mineshige, S. 1992, *MNRAS*, 258, 189  
 Rybicki, G.B., & Lightman, A.P. 1979, *Radiative Processes in Astrophysics*, (New York: Wiley)  
 Shakura, N. I., & Sunyaev, R. A. 1973, *A&A* 24, 337  
 Shakura, N. I., & Sunyaev, R. A. 1976, *MNRAS* 175, 613  
 Shaviv, G., & Wehrse, R. 1986, *A&A*, 259, L5  
 Shimura, T., & Takahara, F. 1993, *ApJ*, 419, 78  
 Turner, T.J. & Pounds, K.A. 1989, *MNRAS* 240, 883